



Implicit level set schemes for modeling hydraulic fractures using the XFEM



Elizaveta Gordeliy, Anthony Peirce*

Department of Mathematics, University of British Columbia, Vancouver, British Columbia V6T 1Z2, Canada

ARTICLE INFO

Article history:

Received 28 February 2013
 Received in revised form 13 July 2013
 Accepted 27 July 2013
 Available online 20 August 2013

Keywords:

XFEM
 Hydraulic fractures
 Level set methods

ABSTRACT

We describe two novel XFEM schemes for modeling fluid driven fractures both of which exploit an implicit level set algorithm (ILSA) for locating the singular free boundary that occurs when the fluid and fracture fronts coalesce. Both schemes use the mixed P&W XFEM formulation developed in Gordeliy and Peirce (2013) [1] to incorporate the singular asymptotic solution in the fracture tips. The proposed level set strategy also exploits the asymptotic solution to provide a robust procedure to locate the free boundary, which is not restricted to symmetric growth of the fracture geometry or to a particular mode of propagation. The versatility of the ILSA-XFEM scheme is demonstrated by sampling different asymptotic behaviors along the so-called MK edge of parameter space (Detournay, 2004) [2] by making use of a universal asymptote (Garagash, 1998 [3]; Garagash and Detournay, 2000 [4]). The two ILSA-XFEM schemes differ in the enrichment strategies that they use to represent the fracture tips: a scheme with full tip enrichment and a simpler, more efficient, scheme in which the tip asymptotic behavior is only imposed in a weak sense. Numerical experiments indicate that the XFEM- t scheme, with full tip enrichment, achieves an $O(h^2)$ asymptotic convergence rate, while the XFEM- s scheme, with only signum enrichment to represent the crack geometry, achieves an $O(h)$ asymptotic convergence rate.

Crown Copyright © 2013 Published by Elsevier B.V. All rights reserved.

1. Introduction

Hydraulic fractures (HF) are cracks that are induced to propagate in solid media due to the injection of viscous fluids. HF occur both naturally, e.g., magma intrusions from pressurized chambers [5] or the drainage of water under glaciers [6], and are used in a growing number of geological engineering applications, e.g. to pre-fracture ore-bodies to enhance continuous block-caving in mining [7,8]; to enhance fracture networks in geothermal reservoirs as well as in oil and gas reservoirs to enhance the recovery of hydrocarbons [9,10]; for waste disposal and the remediation of contaminated soils by the injection of oxidizing reagents [11,12]. Recently in the oil and gas industry there has been considerable deployment of HF in so-called unconventional gas reservoirs that have extensive natural fractures in a rock mass dominated by shales with a fine laminated structure. There is thus considerable interest in being able to model propagating HF within the framework of the finite element method, which is well established as a flexible tool for modeling complex heterogeneous material behavior. The relatively recently developed XFEM [13–15] has great potential for the efficient numerical modeling of propagating HF within the FEM paradigm.

The mathematical model for propagating HF involves coupling the quasi-static equilibrium equations for the impermeable elastic medium with the Reynolds lubrication equation, which expresses the conservation of the viscous fluid within the crack, whose velocity, averaged over the width of the crack, is related to the pressure gradient via Poiseuille's law. Although the 2D elastic equilibrium equations are local PDEs, when the problem is expressed in terms of variables defined along the crack curve in the form of the crack opening displacement and the fluid pressure applied to the faces of the crack, the model equations are reduced by one dimension but are nonlocal in the sense that the pressure field at one point of the crack depends not only on the crack width at that point, but also on the crack widths at all other points of the crack. The model is further complicated by the fact that the Reynolds equation is a degenerate PDE and the fact that the crack geometry is not known *a priori*. Furthermore, if the fluid fills the crack, so that the fluid front does not lag behind the fracture front, but rather the two fronts coalesce, then the fluid pressure field at the tip of such a propagating fracture is typically singular.

Until the recent paper by the authors [1] there had been very little published on XFEM models of HF with full elasto-hydrodynamic coupling. In that paper, the free boundary was located in space–time by specifying fixed fracture growth increments in space and determining the corresponding time-step. This approach is limited to symmetric situations in which the prescribed growth increments at both fracture tips are assumed to occur at the same

* Corresponding author. Tel.: +1 604 822 2104.
 E-mail address: peirce@math.ubc.ca (A. Peirce).

time. Naturally, this situation does not generalize to problems in which the growth rate at the fracture tips is different. In addition, the time-step was found to be weakly dependent on the fracture toughness, which makes the location of the appropriate time-step prone to numerical instability. The objective of the current paper is to explore an alternative methodology for locating the free boundary, which is not restricted to symmetric situations and which is more robust when the pressure field is singular at the fracture tips. In this case estimating the front velocity from Poiseuille's law involves the numerical evaluation of an indeterminate form, in which the square of the vanishing width field is multiplied by the gradient of the singular pressure field, which tends to infinity as the distance to the crack tip is decreased. This singular behavior precludes the use of standard front location methods commonly used for free boundary problems, such as: front tracking, the volume of fluid method, and the level set method, all of which require an accurate velocity field.

To obtain a more general free boundary location scheme, we assume that the time-step is prescribed and that the fracture free boundary points are located by an implicit level set algorithm (ILSA) [16]. This implicit level set methodology was developed for a scheme in which a displacement discontinuity method (DDM) was used to provide a solution of the elastic component of the HF problem. It uses the tip behavior of the crack opening displacement, obtained from detailed asymptotic analysis, to determine the location of the unknown fracture boundary as well as to prescribe the crack opening in the tip elements. Because of the characteristics of the XFEM solution to the elastic crack problem, the implicit level set methodology cannot be applied directly to the HF propagation problem. In [17] it was established that the XFEM, with the appropriate enrichment, provides an $O(h^2)$ solution to the Neumann to Dirichlet Map in which pressures applied to the fracture surfaces are prescribed and the XFEM is used to determine the corresponding crack opening displacement – or crack widths. Conversely, the XFEM, even with the appropriate enrichment, only provides an $O(h)$ solution to the Dirichlet to Neumann Map, in which a prescribed width field is used to determine the corresponding pressure field. In order to use the implicit level set methodology along with an XFEM representation of the elastic crack component of the HF problem, it is necessary to use the P&W mixed boundary value formulation (see [1,17]) of the crack problem in order to incorporate the asymptotic width fields within the tip elements that are typically not differentiable at the fracture front. Away from the crack tips, within the so-called *channel region*, the pressure field is obtained from the lubrication equation and is in turn used to determine the crack opening in the XFEM component of the P&W scheme. This mixed decomposition of the boundary value problem makes it possible to take advantage of the superior accuracy of the Neumann to Dirichlet Map to determine accurate widths within the channel region, which comprises the bulk of the crack.

The implicit level set algorithm assumes a trial fracture front position and that the corresponding fracture widths and fluid pressures have been determined by solving the mixed, coupled lubrication and elasticity equations. The trial fracture opening, in the closest channel element to the fracture tip, is then used to estimate the distance to the fracture boundary points by inverting the local asymptotic expansion for the fracture width as a function of the distance from the tip. If this estimate of the location of the fracture boundary differs from that of the trial fracture front, then the trial front position is updated. This process is repeated until the near-tip width field is consistent with the location of the free boundary – at which time the process is deemed to have converged.

Updating the location of the fracture tips requires a complete update of the contributions to the stiffness matrix of those elements for which the intersection with the fracture has changed or elements that are intersected by the crack for the first time,

and for all neighboring elements at the crack tip that have crack tip enrichment. The computational burden for those elements requiring crack tip enrichment is particularly cumbersome due to the additional integrals involving singular terms that need to be evaluated. In the case of the ILSA-DDM it was found that it is possible to use a crude representation of the tip asymptotic behavior – namely that the average crack opening in the tip element matches the fluid volume given by the asymptotic tip width. This weak-form imposition of the tip asymptotic behavior was found to give remarkably good results. In this paper, in addition to an ILSA-XFEM approach, which uses the full enrichment appropriate for the mode of propagation under consideration, we have developed a similar approach to the ILSA-DDM within the XFEM framework in which we dispense with any crack tip enrichment other than the sign enrichment required to define the crack geometry. The performance of these two different ILSA-XFEM approaches is compared in the numerical experiments presented.

In Section 2, we describe the governing elasto-hydrodynamic equations and their non-dimensionalization. In Section 3, we describe the mixed P&W XFEM formulation used in the construction of the coupled HF algorithm suitable for modeling singular free boundary problems in which there is no fluid lag; we describe two distinct discretizations of the elasto-hydrodynamic equations one including full enrichment at the crack tips and the other in which the crack tips are described using only sign enrichment and prescribed crack opening displacements that can be imposed in a weak sense to only part of the last tip elements; we also describe the level set algorithm used to locate the free boundary. In Section 4, we present the results of numerical experiments in which we compare these XFEM solutions to published reference solutions along the so-called MK edge for dimensionless toughnesses $\mathcal{K} = 0, 1, 2,$ and 3 [18,19]. This class of reference solutions was chosen to illustrate the versatility of the level set approach at locating the free boundary for a specified time-step and which is not restricted to symmetric fracture growth increments. In these numerical examples the performance of the scheme with full tip enrichment is compared to that of the scheme in which only sign enrichment is used throughout the crack. We also perform a convergence study in which the XFEM solutions are compared to the so-called M vertex solution for $\mathcal{K} = 0$ [18]. Finally, we present results of a simulation in which a hydraulic fracture propagates through a bi-material interface.

2. Problem formulation

2.1. Plane strain model

We follow the formulation presented in [1]. Consider a hydraulic fracture propagating in an impermeable elastic medium in a state of plane strain whose stiffness is characterized by the Young's modulus E and Poisson's ratio ν (see Fig. 1), and whose breaking strength is characterized by the fracture toughness K_{Ic} . The fracture is assumed to be driven by the injection of a Newtonian fluid, having a dynamic viscosity μ , from a point source located at the origin of the coordinate system (X, Y) , at a constant volumetric rate Q_0 per unit length in the out-of-plane direction. In two dimensions, the fracture geometry is represented by a curve $\Sigma(t)$ evolving with time t . Along $\Sigma(t)$ we introduce a curvilinear coordinate s , whose origin $s = 0$ is located at the fluid source. For convenient comparison with published reference solutions and for the sake of brevity, we present a formulation of the problem in which the fracture grows symmetrically with respect to the fluid source so that its two wings are characterized by the length $\ell(t)$ and the crack width $w(s, t)$, where $-\ell(t) < s < \ell(t)$. However, the algorithms we describe do not exploit the symmetry of the problem and are used, with trivial modification, to model the non-symmetric crack growth in which a

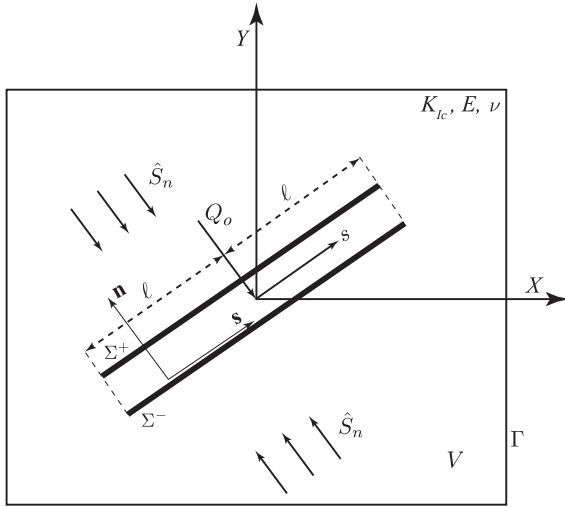


Fig. 1. This figure represents a hydraulic fracture of length 2ℓ that is assumed to grow along the curve Σ within the solid medium occupying the region V with boundary Γ due to the injection of a viscous fluid at a rate Q_o . The fracture depicted is assumed to be subject to a normal confining stress \hat{S}_n only and no shear stress.

hydraulic fracture propagates towards a bi-material interface, which is presented in Section 4.7. During the propagation of hydraulic fractures it is possible that the fluid may lag behind the fracture tips, which results in two moving fluid fronts within the fracture that are located at $s = \pm \ell_f(t)$. Other than the additional work tracking the fluid fronts $\ell_f(t)$, the presence of a non-zero fluid lag is in fact simpler to model than the situation in which the fluid and fracture fronts coalesce, i.e., $\ell_f(t) = \ell(t)$. In this paper we restrict ourselves to this latter case because it involves a singular free boundary problem, which is the more challenging situation for the front location algorithm. The medium is also assumed to be subjected to a uniform stress state (such as the ambient geological confining stress) that can equivalently be represented by normal and shear tractions applied along the crack, denoted by $\hat{S}_n(s)$ and $\hat{S}_s(s)$. The solution to this moving boundary problem involves determining: the complete fracture curve $\Sigma(t)$, the fracture width $w(s, t)$, and the net pressure $p(s, t) = p_f(s, t) - \hat{S}_n(s)$ throughout the fracture $(-\ell(t) < s < \ell(t))$, in which $p_f(s, t)$ is the fluid pressure, for a specified time t within the interval $(0, T)$.

Finally, throughout the paper it is convenient to employ scaled material parameters K' , E' and μ' , defined by

$$K' = 4 \left(\frac{2}{\pi} \right)^{1/2} K_{Ic}, \quad E' = \frac{E}{1 - \nu^2}, \quad \mu' = 12\mu \quad (1)$$

2.2. Governing equations

2.2.1. Elasticity equations and corresponding boundary conditions

The displacement field \mathbf{U} and the stress field \mathbf{S} in the domain are defined with respect to the Cartesian coordinate system (X, Y) (see Fig. 1) centered at the fluid source point and are represented by the components U_i and S_{ij} , respectively. The equilibrium equation, in the absence of body forces, and Hooke's law for the linear elastic medium can be written in the following tensor form

$$\nabla \cdot \mathbf{S} = \mathbf{0} \quad (2)$$

$$\mathbf{S} = \mathbf{C} : \mathbf{E}(\mathbf{U}) \quad (3)$$

in which \mathbf{C} is the tensor of elastic constants, and $\mathbf{E}(\mathbf{U})$ is the strain tensor associated with the displacement \mathbf{U} ,

$$\mathbf{E}(\mathbf{U}) = \frac{1}{2} (\nabla \mathbf{U} + (\nabla \mathbf{U})^T) \quad (4)$$

The domain is denoted by V , while its outer boundary is denoted by Γ , and the fracture surface is denoted by Σ (see Fig. 1). At the outer boundary Γ , the displacement is assumed to be given by a known function $\mathbf{G}(X, Y)$,

$$\mathbf{U}|_{\Gamma} = \mathbf{G} \quad (5)$$

The two crack faces are identified as Σ^+ and Σ^- , and the values of the displacement and the stress along each face are denoted by \mathbf{U}^+ and \mathbf{U}^- and by \mathbf{S}^+ and \mathbf{S}^- , respectively. The unit normal and tangent vectors along the crack are denoted by \mathbf{n} and \mathbf{s} , respectively, and are oriented as shown in Fig. 1. This definition of \mathbf{n} and \mathbf{s} is consistent with the outward normal direction for the crack face Σ^- .

The normal displacement jump at a point s along the crack is equal to the crack width,

$$[[\mathbf{U}]]_{\Sigma} \cdot \mathbf{n} = (\mathbf{U}^+ - \mathbf{U}^-) \cdot \mathbf{n} = w(s, t) \quad (6)$$

Since the normal and shear tractions are continuous across the crack, the normal traction S_n is equal to the net pressure (but opposite in sign), and the shear traction S_s is equal to the applied shear stress. These constraints result in the conditions:

$$S_n^+ = S_n^- = -p(s, t), \quad S_s^+ = S_s^- = \hat{S}_s(s) \quad (7)$$

Here the superscript $+$ or $-$ again denotes the crack face along which the stress component is computed. The normal and the shear tractions are obtained from the stress tensor as $S_n^{\pm} = \mathbf{n}^T (\mathbf{S}^{\pm} \cdot \mathbf{n})$ and $S_s^{\pm} = \mathbf{s}^T (\mathbf{S}^{\pm} \cdot \mathbf{n})$.

2.2.2. Lubrication equation and corresponding boundary conditions

The fluid flux within the fracture, $q(s, t)$, is assumed to be related to the fluid pressure gradient and the fracture width via Poiseuille's law,

$$q = -\frac{w^3}{\mu'} \frac{\partial p_f}{\partial s} \quad (8)$$

and must satisfy the conservation law,

$$\frac{\partial w}{\partial t} + \frac{\partial q}{\partial s} = Q_o \delta(s) \quad (9)$$

Here $\delta(s)$ is the Dirac Delta function, which represents the fluid input into the fracture from a point source located at the origin $s = 0$. By combining (8) and (9), the Reynolds lubrication equation is obtained,

$$\frac{\partial w}{\partial t} = \frac{1}{\mu'} \frac{\partial}{\partial s} \left(w^3 \frac{\partial p_f}{\partial s} \right) + Q_o \delta(s) \quad (10)$$

The boundary conditions for the fluid flow include the conditions that the fracture width and fluid flux vanish at the crack tips, namely:

$$w(\pm \ell(t), t) = 0, \quad q(\pm \ell(t), t) = 0 \quad (11)$$

By integrating the local mass balance equation (9) over the crack length and over the time interval since injection started, and using the boundary condition (11), the following expression for the global fluid balance is obtained,

$$\int_{-\ell(t)}^{\ell(t)} w(s, t) ds = Q_o t \quad (12)$$

2.2.3. Propagation condition and tip asymptotics

Eqs. (2)–(11) would provide a closed system sufficient to determine the fracture width and the fluid pressure if the fracture half-length $\ell(t)$ was known. An additional constraint, required for locating the moving boundary $\ell(t)$, is given by the propagation condition, which is typically formulated in terms of the asymptotic behavior of the fracture width at the crack tips. The appropriate

asymptotic relationship between the fracture width w and the distance from the fracture tip \hat{s} depends upon the regime in which a hydraulic fracture is propagating. The propagation regime is, in turn, determined by the relative importance of two competing dissipative processes, namely: the energy required to break the rock, which is characterized by the rock toughness; and the energy dissipated by driving the viscous fluid through the fracture, which is characterized by the fluid viscosity. These two limiting regimes of hydraulic fracture propagation are associated with the following explicit relationships between w and \hat{s} :

(i) *the toughness dominated regime* (the K-vertex solution, see [4]), is characterized by the classic square root behavior of Linear Elastic Fracture Mechanics [20]

$$w \sim \frac{K'}{E'} \hat{s}^{1/2}, \quad \frac{\hat{s}}{\hat{L}_{mk}} < \hat{\zeta}_k = 10^{-5} \quad (13)$$

where \hat{L}_{mk} is an intermediate length scale defined below;

(ii) *the viscosity dominated regime* (the M-vertex solution, see [21]), is characterized by the asymptotic behavior

$$w \sim \beta_m \left(\frac{\mu' V}{E'} \right)^{1/3} \hat{s}^{2/3}, \quad \frac{\hat{s}}{\hat{L}_{mk}} > \hat{\zeta}_m = 1 \quad \text{and} \quad \beta_m = 2^{1/3} 3^{5/6} \quad (14)$$

The appropriate asymptotic solution, which spans these two limiting asymptotes, can also be obtained from the solution for a semi-infinite crack steadily propagating with a constant tip velocity V [3,4]. Introducing the scalings $\hat{s} = \hat{L} \zeta$, $w(\hat{s}) \sim \hat{W} \hat{\Omega}(\hat{\zeta})$ and $p(\hat{s}) \sim \hat{P} \hat{\Pi}(\hat{\zeta})$ for this problem, the dimensionless groups

$$\hat{G}_m = \frac{\mu' V / E'}{\hat{W}^3 / \hat{L}^2} = \frac{\hat{L}_m}{\hat{W}^3 / \hat{L}^2}, \quad \hat{G}_k = \frac{K' / E'}{\hat{W} / \hat{L}^{1/2}} = \frac{\hat{L}_k^{1/2}}{\hat{W} / \hat{L}^{1/2}} \quad (15)$$

can be identified in which \hat{L}_k is the toughness length scale and \hat{L}_m is the viscous length scale defined by

$$\hat{L}_k = \left(\frac{K'}{E'} \right)^2, \quad \hat{L}_m = \frac{\mu' V}{E'}$$

The intermediate scaling, for which the toughness and viscous effects carry equal weight, is obtained by equating $\hat{G}_m = 1 = \hat{G}_k$, which yields the intermediate length, width, and pressure scales \hat{L}_{mk} , \hat{W}_{mk} and \hat{P}_{mk} that can be expressed in the form

$$\hat{L}_{mk} = \hat{L}_k^{2/3} / \hat{L}_m^{1/3}, \quad \hat{W}_{mk} = \hat{L}_k^{1/3} / \hat{L}_m^{1/3}, \quad \hat{P}_{mk} = E' \hat{L}_m / \hat{L}_k \quad (16)$$

Using this intermediate scaling, $w(\hat{s}) \sim \hat{W}_{mk} \hat{\Omega}_{mk}(\hat{\zeta}_{mk})$ and $\hat{s} = \hat{L}_{mk} \hat{\zeta}_{mk}$ imply the following universal asymptotic behavior

$$w \sim \frac{\hat{L}_k^2}{\hat{L}_m} \hat{\Omega}_{mk} \left(\frac{\hat{L}_m \hat{s}}{\hat{L}_k^2} \right), \quad \hat{s} \rightarrow 0 \quad (17)$$

In Fig. 2 we plot the universal asymptote $\hat{\Omega}_{mk}(\hat{\zeta}_{mk})$, the toughness asymptote $\hat{\Omega}_{mk}(\hat{\zeta}_{mk}) \sim \hat{\zeta}_{mk}^{1/2}$ for $\hat{\zeta}_{mk} \rightarrow 0$ corresponding to (i) above, and the viscous asymptote $\hat{\Omega}_{mk}(\hat{\zeta}_{mk}) \sim \beta_m \hat{\zeta}_{mk}^{2/3}$ for $\hat{\zeta}_{mk} \rightarrow \infty$ and $\beta_m = 2^{1/3} 3^{5/6}$ corresponding to (ii).

2.3. Scaling

The governing equations can be rewritten in a dimensionless form by following a scaling procedure similar to that described in [2]. In order to achieve this, the following dimensionless variables are introduced,

$$t = t_* \tau, \quad X = \ell_* x, \quad Y = \ell_* y, \quad s = \ell_* \zeta, \quad \ell(t) = \ell_* \gamma(\tau) \quad (18)$$

$$w(s, t) = w_* \Omega(\zeta, \tau), \quad p(s, t) = p_* \Pi(\zeta, \tau) \quad (19)$$

$$q(s, t) = Q_0 \Psi(\zeta, \tau) \quad (20)$$

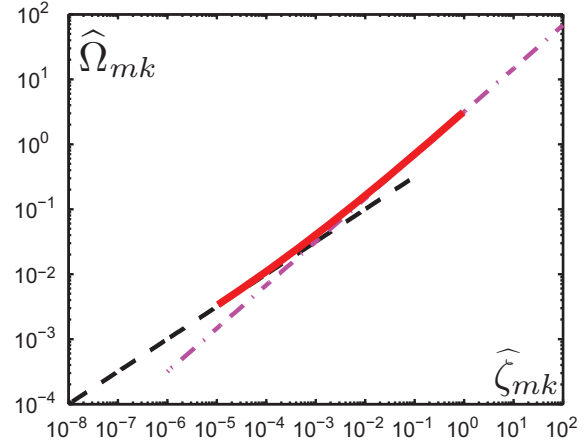


Fig. 2. The stationary solution $\hat{\Omega}_{mk}(\hat{\zeta}_{mk})$ for a semi-infinite fracture propagating with a constant velocity V is denoted by the solid red line. The toughness asymptote, represented by the dashed black line, is valid for $\hat{\zeta}_{mk} \lesssim \hat{\zeta}_k = 10^{-5}$. The viscous asymptote, represented by the dash-dotted magenta line, is valid for $\hat{\zeta}_{mk} \gtrsim \hat{\zeta}_m = 1$. (For interpretation of the references to color in this figure legend, the reader is referred to the web version of this article.)

$$\mathbf{U}(X, Y) = w_* \mathbf{u}(x, y), \quad \mathbf{S}(X, Y) = p_* \boldsymbol{\sigma}(x, y) \quad (21)$$

$$\hat{S}_n = p_* \hat{\sigma}_n, \quad \hat{S}_s = p_* \hat{\sigma}_s \quad (22)$$

where t_* , ℓ_* , w_* and p_* are the characteristic scales for the time, the length, the crack width, and the net pressure that are active in the problem. The dimensionless variables are: the time τ , the Cartesian coordinates (x, y) , the tangential coordinate along the crack ζ , the crack half-length γ , the net pressure Π , the fluid pressure Π' , the crack width Ω , the fluid flux Ψ , the displacement \mathbf{u} and the stress $\boldsymbol{\sigma}$.

When the governing equations are reformulated in terms of these dimensionless variables, the following four dimensionless groups can be identified in the governing equations:

$$\mathcal{G}_e = \frac{p_* \ell_*}{E' w_*}, \quad \mathcal{G}_v = \frac{Q_0 t_*}{w_* \ell_*}, \quad \mathcal{G}_m = \frac{\mu' \ell_* Q_0}{w_*^3 p_*}, \quad \mathcal{G}_k = \frac{K' \ell_*^{1/2}}{E' w_*} \quad (23)$$

In order to reformulate the governing equations in terms of dimensionless variables that are of order one, three of these groups are set to 1. These three constraints combined with a characteristic length or time scale of interest, such as the maximum fracture length expected in the simulation or the specified maximum injection time T , are used to identify the four characteristic scales t_* , ℓ_* , w_* and p_* . Proceeding in this way two distinct scalings emerge:

- **Toughness scaling:** $\mathcal{G}_e = \mathcal{G}_v = \mathcal{G}_k = 1$. Combining these three conditions with the definitions of the dimensionless groups (23), we obtain the following power-law relationships between the characteristic length, width, pressure and the characteristic time scale t_* :

$$\begin{aligned} \ell_k &= \left(\frac{E' Q_0}{K'} \right)^{2/3} t_*^{2/3}, \quad w_k = \left(\frac{K'^2 Q_0}{E'^2} \right)^{1/3} t_*^{1/3}, \quad p_k \\ &= \left(\frac{K'^4}{E' Q_0} \right)^{1/3} t_*^{-1/3} \end{aligned} \quad (24)$$

The dimensionless viscosity in this scaling $\mathcal{G}_m = \frac{\mu' E'^3 Q_0}{K'^4} := \mathcal{M}$ is considered a parameter.

- **Viscosity scaling:** $\mathcal{G}_e = \mathcal{G}_v = \mathcal{G}_m = 1$. Combining these three conditions with the definitions of the dimensionless groups (23), we obtain the following power-law relationships between the characteristic length, width, and pressure and the characteristic time scale t_* :

$$\begin{aligned} \ell_m &= \left(\frac{E' Q_0^3}{\mu'} \right)^{1/6} t_*^{2/3}, \quad w_m = \left(\frac{\mu' Q_0^3}{E'} \right)^{1/6} t_*^{1/3}, \quad p_m \\ &= (\mu' E^2)^{1/3} t_*^{-1/3} \end{aligned} \quad (25)$$

The dimensionless toughness in this scaling $\mathcal{G}_k = \left(\frac{\mu' K^4}{E^3 Q_0} \right)^{1/4} := \mathcal{K} = \mathcal{M}^{-1/4}$ is considered a parameter.

The governing equations and boundary conditions can then be rewritten in the following dimensionless form:

- Equilibrium equation

$$\nabla \cdot \boldsymbol{\sigma} = \mathbf{0} \quad (26)$$

- Hooke's law

$$\boldsymbol{\sigma} = \mathcal{C} : \boldsymbol{\varepsilon}(\mathbf{u}) \quad (27)$$

in which \mathcal{C} is the scaled elasticity tensor, $\mathcal{C} = \mathbf{C}/E'$, and $\boldsymbol{\varepsilon}(\mathbf{u})$ is the strain tensor associated with the scaled displacement \mathbf{u} and scaled coordinates (x, y) ,

$$\boldsymbol{\varepsilon}(\mathbf{u}) = \frac{1}{2} (\nabla_{xy} \mathbf{u} + (\nabla_{xy} \mathbf{u})^T) \quad (28)$$

- Boundary conditions for the displacement and stress fields

$$\mathbf{u}|_{\Gamma} = \mathbf{g} \quad (29)$$

$$[[\mathbf{u}]]_{\Sigma} \cdot \mathbf{n} = (\mathbf{u}^+ - \mathbf{u}^-) \cdot \mathbf{n} = \Omega(\zeta, \tau) \quad (30)$$

$$\sigma_n^+ = \sigma_n^- = -\Pi(\zeta, \tau), \quad \sigma_s^+ = \sigma_s^- = \hat{\sigma}_s(\zeta) \quad (31)$$

where $\mathbf{g} = \mathbf{G}/w$, is the scaled prescribed displacement at the outer boundary Γ , and $\sigma_{\eta}^{\pm} = S_{\eta}^{\pm}/p_s$ for $\eta = n, s$ are the scaled normal and shear stresses;

- Poiseuille's law

$$\Psi = -\Omega^3 \frac{\partial \Pi^f}{\partial \zeta} \quad (32)$$

- Conservation law

$$\dot{\Omega} + \frac{\partial \Psi}{\partial \zeta} = \delta(\zeta) \quad (33)$$

where we use the notation $\dot{\Omega} = \frac{\partial \Omega}{\partial \tau}$.

- Boundary conditions at the crack tips

$$\Omega(\pm\gamma, \tau) = 0, \quad \Psi(\pm\gamma, \tau) = 0 \quad (34)$$

- The Reynolds lubrication equation

$$\dot{\Omega} = \frac{\partial}{\partial \zeta} \left(\Omega^3 \frac{\partial \Pi^f}{\partial \zeta} \right) + \delta(\zeta) \quad (35)$$

- The global volume balance condition

$$\int_{-\gamma}^{\gamma} \Omega d\zeta = \tau \quad (36)$$

- The Propagation condition using the universal asymptote: In order to map the tip behavior of a finite fracture to that of the universal M-K asymptote defined in (17), we identify V with the instantaneous velocity of the finite fracture, which, in the viscous scaling, reduces to the form $V = \ell = \frac{\ell_m}{t_*} \dot{\gamma}(\tau)$. Now $w = w_m \Omega(\hat{\zeta}) = \widehat{W}_{mk} \widehat{\Omega}_{mk}(\hat{\zeta}_{mk})$ and $\hat{s} = \ell_m \hat{\zeta} = \widehat{L}_{mk} \hat{\zeta}_{mk}$ along with the above relation between V and $\dot{\gamma}$ yields the appropriate mapping from $\widehat{\Omega}_{mk}$ to Ω

$$\Omega \sim \frac{\mathcal{K}^4}{\dot{\gamma}(\tau)} \widehat{\Omega}_{mk} \left(\frac{\dot{\gamma}(\tau)^2}{\mathcal{K}^6} \hat{\zeta} \right), \quad \hat{\zeta} \ll 1 \quad (37)$$

From Fig. 2 we see that the limiting toughness asymptote applies when $\hat{\zeta}_{mk} \leq \hat{\zeta}_k \approx 10^{-5}$ so that:

$$\Omega \sim \mathcal{K} \hat{\zeta}^{1/2}, \quad \frac{\dot{\gamma}(\tau)^2}{\mathcal{K}^6} \hat{\zeta} \leq \hat{\zeta}_k \approx 10^{-5} \quad (38)$$

and the limiting viscous asymptote applies when $\hat{\zeta}_{mk} \geq \hat{\zeta}_m \approx 10^0$:

$$\Omega \sim \beta_m \dot{\gamma}(\tau)^{1/3} \hat{\zeta}^{2/3}, \quad \frac{\dot{\gamma}(\tau)^2}{\mathcal{K}^6} \hat{\zeta} \geq \hat{\zeta}_m \approx 10^0 \quad (39)$$

Here, $\hat{\zeta}$ is the scaled distance from the crack tip: $\hat{\zeta} = \gamma \pm \zeta$ when the neighborhood of the crack tip is at $\zeta = \mp \gamma$, respectively.

3. The ILSA-XFEM scheme for propagating hydraulic fractures

3.1. Mixed P&W XFEM scheme for a crack in an elastic medium

In this paper we use the mixed P&W scheme (see [17]) in which the crack opening displacement in a neighborhood Σ_t of the crack tip is prescribed while the pressure is prescribed in the interior of the crack $\Sigma_c = \Sigma \setminus \Sigma_t$:

$$\Omega(\zeta) = \Omega_t(\zeta), \quad \zeta \in \Sigma_t; \quad \Pi(\zeta) = \Pi_c(\zeta), \quad \zeta \in \Sigma_c \quad (40)$$

The appropriate XFEM formulation is then used to determine the crack opening displacement along Σ_c . Estimates of the pressure field within the neighborhood Σ_t of the tip can also be determined, however these are likely to be inaccurate due to the singular nature of the pressure field at the tip. Instead of using the pressure field that has been determined from the elasticity equation, the pressure in the tip elements is determined from the lubrication equation by matching the flux to the change in the asymptotic tip volume that has occurred over the given time step $\Delta\tau$. The so-called $P \rightarrow W$ scheme, which was also described in [17], is only suitable for problems with a fluid lag in which the fluid pressure is finite at the fluid front and will not be discussed in this paper.

3.1.1. Weak formulation

We use the localized mixed hybrid formulation introduced by Zilian and Fries [22] to specify the displacement jump Ω_t along that part of the domain which is adjacent to the crack boundary Σ_t , and follow the formulation described in [23] for the rest of the domain. The domain V is discretized into a mesh \mathcal{F} of non-overlapping quadrilateral elements e each of which occupies the region V_e^h , such that: $V = \bigcup_{e \in \mathcal{F}} V_e^h$. The subset of elements that overlap with that part of the crack Σ_t along which Ω_t is prescribed is denoted \mathcal{B} : $\mathcal{B} = \{e \in \mathcal{F} : V_e^h \cap \Sigma_t \neq \emptyset\}$. The domain V is thus artificially partitioned into two domains: V_o and $\bigcup_{e \in \mathcal{B}} V_e^h$, where $V_o = V \setminus \bigcup_{e \in \mathcal{B}} V_e^h$ contains all elements that do not overlap with Σ_t .

The displacement in V is approximated by elements of the trial space $\mathcal{U}_{\mathbf{u}}^h = \{\mathbf{u}^h | \mathbf{u}^h \in U, \mathbf{u}^h = \mathbf{g} \text{ on } \Gamma\}$ while variations are taken from the test space $\mathcal{V}_{\mathbf{u}}^h = \{\mathbf{v}^h | \mathbf{v}^h \in U, \mathbf{v}^h = \mathbf{0} \text{ on } \Gamma\}$. Here U is a finite-dimensional subspace of the Sobolev space $H^1(V \setminus \Sigma) \times H^1(V \setminus \Sigma)$ that consists of the shape functions representing the discretization \mathbf{u}^h . The domain $V \setminus \Sigma$ that does not contain the crack Σ is assumed to be piecewise Lipschitz. The test and trial functions are assumed to be discontinuous in a direction normal to the crack Σ .

For a test or trial function \mathbf{u}^h , the corresponding strain $\boldsymbol{\varepsilon}(\mathbf{u}^h)$ is computed from (28), while the corresponding stress can be obtained from Hooke's law (27) to yield $\boldsymbol{\sigma}(\mathbf{u}^h) = \mathcal{C} : \boldsymbol{\varepsilon}(\mathbf{u}^h)$. However, in each element $e \in \mathcal{B}$, the stress $\boldsymbol{\sigma}$ is introduced as an auxiliary tensor variable for which Hooke's law (27) is weakly imposed. Following [22] we approximate $\boldsymbol{\sigma}$, by introducing the test (and trial) tensor function space

$$S_\sigma^h = \{\sigma^h | \sigma_{ij}^h = \sigma_{ji}^h, \sigma_{ij}^h \in H^{-1h} \text{ for } i = 1, 2 \text{ and } j = 1, 2\}$$

in which H^{-1h} is a finite-dimensional subspace of the space of functions that are square-integrable in each element in B and which are discontinuous at the element edges and in a direction normal to the crack Σ . In the next subsection we define the shape functions for this subspace on the element level for each $e \in B$.

The discretized formulation of the elasticity problem (26)–(31), (40) seeks to find $(\mathbf{u}^h, \boldsymbol{\sigma}^h) \in \mathcal{U}_u^h \times S_\sigma^h$ such that, for all $(\mathbf{v}^h, \boldsymbol{\tau}^h) \in \mathcal{V}_u^h \times S_\sigma^h$,

$$0 = \int_{V_0 \setminus \Sigma} \boldsymbol{\varepsilon}(\mathbf{v}^h) : \boldsymbol{\sigma}(\mathbf{u}^h) dV + \int_{\Sigma_c} [[\mathbf{v}^h]] \cdot (-\Pi_c(\zeta) \mathbf{n} + \hat{\sigma}_s(\zeta) \mathbf{s}) d\zeta \quad (41)$$

$$+ \sum_{e \in B} \int_{V_e^h \setminus \Sigma} \boldsymbol{\varepsilon}(\mathbf{v}^h) : \boldsymbol{\sigma}^h dV + \sum_{e \in B} \int_{V_e^h \setminus \Sigma} \boldsymbol{\tau}^h : (\boldsymbol{\varepsilon}(\mathbf{u}^h) - \mathbf{C}^{-1} : \boldsymbol{\sigma}^h) dV \quad (42)$$

$$+ \sum_{e \in B} \int_{\Sigma_{t,e}} ([[\mathbf{v}^h]] \cdot \mathbf{n})(\mathbf{n} \cdot \{ \boldsymbol{\sigma}^h \} \cdot \mathbf{n}) + (\mathbf{n} \cdot \{ \boldsymbol{\tau}^h \} \cdot \mathbf{n})([[\mathbf{u}^h]] \cdot \mathbf{n} - \Omega_t(\zeta)) + ([[\mathbf{v}^h]] \cdot \mathbf{s}) \hat{\sigma}_s(\zeta) d\zeta \quad (43)$$

where $\Sigma_{t,e} = \Sigma_t \cap V_e^h$; here $\{ \cdot \}$ denotes the averaged quantity obtained from the two crack faces Σ^\pm , i.e., $\{ \boldsymbol{\sigma} \} = \frac{1}{2}(\boldsymbol{\sigma}^+ + \boldsymbol{\sigma}^-)$, and $[[\mathbf{v}]] = (\mathbf{v}^+ - \mathbf{v}^-)$ denotes the jump of \mathbf{v} across the crack.

3.1.2. Enrichment: sign and fixed radius tip enrichment

The fundamental idea behind the XFEM is to efficiently represent interfaces and cracks by augmenting the standard set of Lagrange shape functions by specialized enrichment functions in elements around these features. Following [23] cracks are represented by two forms of enrichment, namely sign and tip enrichment, as originally suggested by Moës et al. [13]. Sign enrichment is necessary to define the geometry of the crack while the tip enrichment is required to restore the order of convergence expected of the underlying finite element discretization of the elasticity problem, which degrades due to the presence of the singular behavior at the crack tips. The sign enrichment is relatively inexpensive to implement compared to the tip enrichment, which requires computationally intensive spatial integration of the singular enrichment functions in the tip-enriched elements. In this paper we will consider the performance of the XFEM scheme for modeling propagating HF, with and without tip enrichment. The details of these enrichment strategies are as follows:

- (I) Sign enrichment: the crack geometry is defined by enriching those elements that intersect the crack by the sign function defined as follows:

$$\mathbf{sg}(\mathbf{x}) = \text{sign}(\phi(\mathbf{x})), \quad \mathbf{x} \in V \quad (44)$$

in which $\phi(\mathbf{x}) = \pm \min_{\tilde{\mathbf{x}} \in \tilde{\Sigma}} |\mathbf{x} - \tilde{\mathbf{x}}|$ is the signed distance function that has different signs on the two sides of the crack or its extension $\tilde{\Sigma}$. The curve $\tilde{\Sigma}$ includes the crack and may extend beyond each crack tip, in the direction tangent to the crack, to the farthest edge of the encompassing finite element.

- (II) Tip enrichment: singular behavior at the crack tip is captured by introducing specialized enrichment basis functions that are obtained from special solutions of the elastic equilibrium equations. In this paper we consider a general class of tip asymptotic behavior in the limit as the distance ζ to the fracture tip tends to zero:

$$\Omega_t(\zeta) \stackrel{\zeta \rightarrow 0}{\sim} A \zeta^\lambda, \quad \text{where } \frac{1}{2} \leq \lambda < 1, \quad (45)$$

for some constant A . It can be shown [24] by local analysis of the tip asymptotics that the corresponding pressure behavior is of the form $\Pi_t \stackrel{\zeta \rightarrow 0}{\sim} \frac{1}{4} A \lambda \cot(\pi \lambda) \zeta^{2\lambda-1}$ when $\frac{1}{2} < \lambda < 1$. Consistent with this asymptotic behavior, the appropriate enrichment

basis functions for the displacement and corresponding stress fields are of the form (see [17]):

$$\boldsymbol{\psi}^{\mathbf{u},\lambda} = r^\lambda \{ \sin(\lambda\theta), \cos(\lambda\theta), \sin(\lambda-2)\theta, \cos(\lambda-2)\theta \} \quad (46)$$

$$\boldsymbol{\psi}^{\boldsymbol{\sigma},\lambda} = r^{\lambda-1} \{ \sin(\lambda-1)\theta, \cos(\lambda-1)\theta, \sin(\lambda-3)\theta, \cos(\lambda-3)\theta \} \quad (47)$$

where (r, θ) are polar coordinates centered at the fracture tip, so that the values $\theta = \pm\pi$ correspond to the two crack faces. The tip enrichment comprises the four singular functions $\{ \boldsymbol{\psi}^{\mathbf{u}} \}$ defined in (46) that are used to represent the singular behavior at the fracture tips. This enrichment is introduced at all nodes that are within a prescribed radius ρ from either crack tip \mathbf{x}_{tip} , i.e., $I_t = \{ i \in I : |\mathbf{x}_i - \mathbf{x}_{tip}| \leq \rho \}$, where $\mathbf{x}_i \in V$ denote coordinates of the finite element node i , and I is the set of all nodes. Sign enrichment is introduced for nodes in the set I_s comprising all the nodes of the elements cut by the crack, excluding the nodes already in I_t , so that $I_t \cap I_s = \emptyset$. (For the XFEM without tip enrichment, $I_t = \emptyset$, and the set I_s then comprises all the nodes of the elements cut by the crack.)

The finite-dimensional Galerkin space U is defined by $U = H^{1h} \times H^{1h}$ and is spanned by the following shape functions:

$$H^{1h} = \left\{ \sum_{i \in I} a_i N_i(\mathbf{x}) + R_s(\mathbf{x}) \sum_{i \in I_s^*} b_i N_i(\mathbf{x})(\mathbf{sg}(\mathbf{x}) - \mathbf{sg}(\mathbf{x}_i)) + R_t(\mathbf{x}) \sum_{i \in I_t^*} N_i(\mathbf{x}) \sum_{j=1}^4 c_i^j (\boldsymbol{\psi}_j^{\mathbf{u}}(\mathbf{x}) - \boldsymbol{\psi}_j^{\mathbf{u}}(\mathbf{x}_i)) \right\} \quad (48)$$

where $\mathbf{x} \in V \setminus \Sigma$; N_i are the standard piecewise bi-linear Lagrange basis functions; and $a_i, b_i, c_i^j \in \mathbb{R}$. Here I_s^* is the set of all nodes of elements that are cut by the crack and that have at least one node in I_s , and I_t^* is the set of all nodes in elements that have at least one node in I_t . Naturally, $I_s \subseteq I_s^*, I_t \subseteq I_t^*$, and $I_s^* \cap I_t^* \neq \emptyset$ provided $I_t^* \neq \emptyset$. In addition, if tip enrichment is being used, the two blending functions $R_t(\mathbf{x}) = \sum_{i \in I_t^*} N_i(\mathbf{x})$ and $R_s(\mathbf{x}) = 1 - R_t(\mathbf{x})$ are introduced to blend the two enrichments (see [23,25]) so that the representation (48) maintains the partition of unity property [26], which is sufficient to obtain an optimal convergence rate for the XFEM [27]. For the XFEM without tip enrichment, these degenerate to $I_s^* = I_s, I_t^* = \emptyset, R_t(\mathbf{x}) = 0$ and $R_s(\mathbf{x}) = 1$.

It should be noted that, for the XFEM without tip enrichment, the displacement shape functions (48) are discontinuous along the extended crack $\tilde{\Sigma}$, and the weak form (41)–(43) has to be reformulated for the extended crack $\tilde{\Sigma}$. To keep a unified formulation of the coupled XFEM schemes with different enrichment strategies and to use the weak form (41)–(43) for either enrichment, in the following we use the notation Σ to denote the *extended* crack $\Sigma = \tilde{\Sigma}$ for the XFEM without tip enrichment and the *actual* crack for the XFEM with tip enrichment. In other words, for both enrichment strategies Σ represents the curve over which the shape functions defined in (48) are discontinuous. In particular, for the XFEM without tip enrichment, the line integrals in the tip elements in (43) are computed over the extended elemental tip regions $\Sigma_{t,e} = \Sigma_t \cap V_e^h$, in which Σ_t is the extension of the crack tip region beyond the actual crack tip to the edge of the encompassing finite element, in the direction tangent to the crack. Further details of using the prescribed crack opening displacement $\Omega_t(\zeta)$ in the extended crack tip region are discussed in Section 3.2.

The stress in each element $V_e^h, e \in B$, is represented by the shape functions from the finite-dimensional space H^{-1h} defined on an element level as follows:

- For the XFEM with tip enrichment, we choose the radius of the enrichment ρ so that all nodes of the elements in the set B are located within the distance ρ from the closest crack tip, i.e. $\cup_{e \in B} I_e \subset I_t$, where I_e denotes the set of all nodes in element e .

Hence the displacement shape functions (48) do not involve sign enrichment in the domain $\cup_{e \in \mathcal{B}} V_e^h$, and the stress components can be represented by the four singular functions $\{\psi_j^\sigma\}$ given in (47) and by standard Lagrange basis functions, where $\mathbf{x} \in \cup_{e \in \mathcal{B}} V_e^h \setminus \Sigma$, and $a_i^e, c_i^{j,e} \in \mathbb{R}$:

$$H^{-1h} = \left\{ \cup_{e \in \mathcal{B}} v^e(\mathbf{x}) : v^e(\mathbf{x}) = \sum_{i \in I_e} a_i^e N_i(\mathbf{x}) + \sum_{i \in I_e} N_i(\mathbf{x}) \sum_{j=1}^4 c_i^{j,e} (\psi_j^\sigma(\mathbf{x}) - \psi_j^\sigma(\mathbf{x}_i)) \text{ if } \mathbf{x} \in V_e^h; v^e(\mathbf{x}) = 0 \text{ if } \mathbf{x} \notin V_e^h \right\}$$

- For the XFEM without tip enrichment, the stress components are represented by the sign enrichment and by standard Lagrange basis functions,

$$H^{-1h} = \left\{ \cup_{e \in \mathcal{B}} v^e(\mathbf{x}) : v^e(\mathbf{x}) = \sum_{i \in I_e} a_i^e N_i(\mathbf{x}) + \sum_{i \in I_e} b_i^e N_i(\mathbf{x})(\mathbf{sg}(\mathbf{x}) - \mathbf{sg}(\mathbf{x}_i)) \text{ if } \mathbf{x} \in V_e^h; v^e(\mathbf{x}) = 0 \text{ if } \mathbf{x} \notin V_e^h \right\}$$

where again $\mathbf{x} \in \cup_{e \in \mathcal{B}} V_e^h \setminus \Sigma$; $a_i^e, b_i^e \in \mathbb{R}$; and I_e denotes the set of all nodes in element e .

3.1.3. Infinite elements

In modeling hydraulic fracture propagation in large-scale problems, the boundary conditions at a finite outer boundary are often unknown. This can be resolved by modeling a fracture propagation in an infinite domain, assuming a vanishing displacement at infinity. To represent an infinite domain, we employ mapped infinite elements that make it possible to capture a decaying far-field displacement [28,29]. The details of the infinite elements used in this paper are summarized in [1].

3.2. Discrete coupled equations

The P&W XFEM scheme described above makes it possible to incorporate the asymptotic behavior of the width in the neighborhood of the crack tip as a boundary condition. The advantage of this scheme is that it can treat problems in which the fluid pressure is singular at the crack tips, such as the viscous or toughness modes of propagation for cracks that are completely filled with fluid, i.e., when $\gamma_f = \gamma$ [30,19]. The coupled P&W scheme can easily be applied to the non singular boundary value problems with fluid lag, i.e., when $\gamma_f < \gamma$, however these will not be considered here. In order to facilitate comparison with published reference solutions we only consider the propagation of cracks along straight lines, so that the deflection angle of the crack trajectory at each step of propagation is zero. This assumption does not limit the class of problems that can be solved using the coupled P&W scheme. Indeed, this restriction can be relaxed by incorporating an appropriate search strategy (e.g., for the maximum tensile stress direction in the vicinity of the crack tip) to identify the propagation direction of the crack at each growth increment. Since the crack is assumed to propagate along a straight line, the applied normal stress $\hat{\sigma}_n(\zeta) \equiv \hat{\sigma}_n$ is uniform along the crack and the fluid flow equations

(32) and (35) can be reformulated in terms of the gradient of the net pressure $\frac{\partial \Pi}{\partial \zeta} = \frac{\partial \Pi^f}{\partial \zeta}$. For the problems we consider, we also assume that the shear stress applied along the crack faces vanishes: i.e., $\hat{\sigma}_s = 0$.

The crack is divided into two crack tip regions $\Sigma_t = (\zeta_0, \zeta_1) \cup (\zeta_N, \zeta_{N+1})$ and a channel region $\Sigma_c = (\zeta_1, \zeta_N)$ (see

Fig. 3). In general each tip region can have more than one element, however, to simplify the presentation we assume that the tip regions each comprise only one element. The width in the crack tip

elements is assumed to be governed by the applicable tip asymptote selected from (38), (39) or (37). Thus the P&W XFEM scheme uses the crack width boundary condition in the tip elements, and the pressure boundary condition in the channel region (ζ_1, ζ_N) , according to (40). We consider two versions of the P&W XFEM, namely the P&W XFEM-s scheme, which uses only sign enrichment and no tip enrichment, and the P&W XFEM-t scheme, which uses both sign enrichment and the tip enrichment appropriate to the applicable asymptote.

The P&W XFEM-s scheme: we assume that the sign enrichment is used in all channel elements and in each of the finite elements containing the fracture tips. In the elements containing the fracture tips, the sign enrichment extends in the fracture growth direction, beyond the actual tip of the fracture, to the farthest edge of the finite element (see Fig. 3(a)). The appropriate tip asymptote (38), (39) or (37) is imposed in a weak sense by using this asymptotic behavior for $\Omega_t(\zeta)$ in the tip integral in (43). While the sign enrichment for this case actually extends beyond the tip to the far edge of the encompassing finite element, in this extended region it is assumed that $\Omega_t(\zeta) = 0$ for $|\zeta| > \gamma$, so that there is no contribution from the tip asymptote to the weak form beyond the crack tip.

The P&W XFEM-t scheme: we assume that the sign enrichment covers only the channel elements and that crack tip enrichment is used for the tip elements according to (48) (see Fig. 3(b)). It is also assumed that blending of the two enrichments takes place in the channel. Hence we choose the tip enrichment radius ρ so that elements for which tip enrichment is applied completely cover the tip regions (ζ_0, ζ_1) and (ζ_N, ζ_{N+1}) .

3.2.1. The XFEM solution

The XFEM solution can be represented as a superposition of solutions that approximate the width boundary condition in Σ_t and the pressure boundary condition in Σ_c , given by (40). The aim is to use the nodal net pressures in the channel and the asymptotic

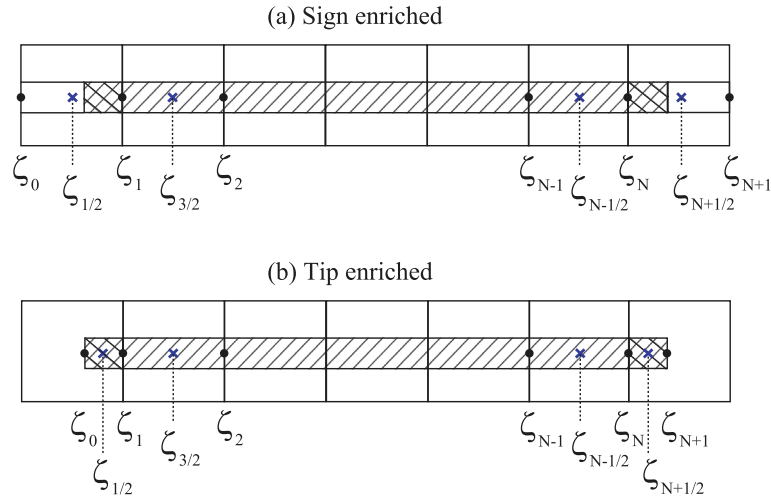


Fig. 3. Discretization of the crack without fluid lag within a regular FEM mesh of square elements. The elements in the channel region Σ_c are single shaded while there is one element in each of the two tip regions Σ_t , which are indicated by double shading.

widths in the tips to reconstruct the appropriate boundary conditions (40) for the XFEM.

In both schemes, we develop approximations of the pressure in terms of the standard piecewise linear Lagrange hat functions associated with the element midpoint nodes $\zeta_{i+1/2} = (\zeta_i + \zeta_{i+1})/2$ (see Fig. 3),

$$h_{i+1/2}(\zeta) = \begin{cases} \frac{\zeta - \zeta_{i-1/2}}{\zeta_{i+1/2} - \zeta_{i-1/2}}, & \text{if } \zeta_{i-1/2} \leq \zeta < \zeta_{i+1/2} \\ \frac{\zeta_{i+3/2} - \zeta}{\zeta_{i+3/2} - \zeta_{i+1/2}}, & \text{if } \zeta_{i+1/2} \leq \zeta < \zeta_{i+3/2} \\ 0, & \text{else} \end{cases} \quad (49)$$

the left edge hat function:

$$h_{1/2}(\zeta) = \begin{cases} \frac{\zeta_{3/2} - \zeta}{\zeta_{3/2} - \zeta_{1/2}}, & \text{if } \zeta_{1/2} \leq \zeta < \zeta_{3/2} \\ 0, & \text{else} \end{cases} \quad (50)$$

and the right edge hat function:

$$h_{N+1/2}(\zeta) = \begin{cases} \frac{\zeta - \zeta_{N-1/2}}{\zeta_{N+1/2} - \zeta_{N-1/2}}, & \text{if } \zeta_{N-1/2} \leq \zeta < \zeta_{N+1/2} \\ 0, & \text{else} \end{cases} \quad (51)$$

At step M of the crack propagation, associated with the given time $\tau = \tau_M$, the net pressure Π is expanded in terms of the hat basis functions $h_{i+1/2}(\zeta)$ associated with the nodal values $\Pi_{i+1/2}$ as follows:

$$\Pi(\zeta, \tau_M) \approx \sum_{i=0}^N \Pi_{i+1/2} h_{i+1/2}(\zeta), \quad \zeta \in \Sigma_c \quad (52)$$

which provides a C^0 -continuous approximation of Π within the channel $\zeta \in \Sigma_c$. In the tip regions, depending on the value of the dimensionless toughness \mathcal{K} , the crack width is approximated by the tip asymptote $\mathcal{W}(\zeta; \dot{\gamma})$ representing one of (38), (39), or (37), and which can be expressed in the following general form involving the fracture front velocity $\dot{\gamma}(\tau)$:

$$\Omega \sim \mathcal{W}(\zeta; \dot{\gamma}), \quad \zeta \rightarrow 0 \quad (53)$$

The front velocity can be approximated by the backward difference approximation $\dot{\gamma} \approx (\gamma - \gamma^0)/\Delta\tau$, where $\Delta\tau$ is the prescribed time-step, γ^0 is the front position at the previous time-step, and γ is the current front position that has to be determined in the coupled solution. For the tip enriched scheme the appropriate power-law exponent λ , which depends on the value of the dimensionless

toughness \mathcal{K} , is employed for the singular tip enrichment within the XFEM.

To implement this scheme it is convenient to construct an influence matrix, which is determined by solving a sequence of mixed elastic boundary value problems. Firstly, the elasticity problem (26)–(29) is solved using the XFEM to generate $N + 1$ width basis functions denoted by $\omega_{i+1/2}(\zeta)$ that represent the jump in the normal displacement across Σ , and which are the solutions to the mixed boundary value problem in which the prescribed pressures in the channel are given by the basis functions $h_{i+1/2}(\zeta)$ for $i = 0 : N$:

$$\sigma_n^+ = \sigma_n^- = -h_{i+1/2}(\zeta) \text{ for } \zeta \in \Sigma_c, \quad \sigma_s^+ = \sigma_s^- = 0 \text{ for } \zeta \in \Sigma \quad (54)$$

and for which the widths in the tip elements are forced to be zero, i.e., $\Omega_t(\zeta) = 0$ for $\zeta \in (\zeta_0, \zeta_1)$ or $\zeta \in (\zeta_N, \zeta_{N+1})$ so that according to (43) we have the weak condition

$$[[\mathbf{u}]]_{\Sigma} \cdot \mathbf{n} = 0 \text{ for } \zeta \in \Sigma_t. \quad (55)$$

Secondly, to represent the influence of the tip widths on the crack opening displacement in the channel region, the following mixed elastic boundary value problem is solved. Using the XFEM, the width function $\omega_t(\zeta)$ is constructed that is a solution to the elasticity problem (26)–(29) with the following boundary conditions

$$\sigma_n^+ = \sigma_n^- = 0 \text{ for } \zeta \in \Sigma_c, \quad \sigma_s^+ = \sigma_s^- = 0 \text{ for } \zeta \in \Sigma \quad (56)$$

and

$$[[\mathbf{u}]]_{\Sigma} \cdot \mathbf{n} = \begin{cases} \mathcal{W}(\zeta + \gamma; \dot{\gamma}) & \text{for } \zeta \in (\zeta_0, \zeta_1) \\ \mathcal{W}(\gamma - \zeta; \dot{\gamma}) & \text{for } \zeta \in (\zeta_N, \zeta_{N+1}) \end{cases} \quad (57)$$

Due to the linearity of the elasticity problem, the width $\Omega(\zeta, \tau_M)$ along the crack corresponding to the pressure (52) and the prescribed tip widths is given by the following linear combination:

$$\Omega(\zeta, \tau_M) \approx \omega_t(\zeta) + \sum_{j=0}^N \Pi_{j+1/2} \omega_{j+1/2}(\zeta) \quad (58)$$

Now evaluating the width basis functions $\omega_{j+1/2}(\zeta)$ at channel nodes ζ_i , $i = 1 : N$, we obtain the influence matrix $D_{ij} = \omega_{j+1/2}(\zeta_i)$. Thus, given the nodal pressures $\Pi_{j+1/2}$, $j = 0 : N$, the XFEM approximation for the nodal widths in the channel can be written in the form

$$\Omega_i = \omega_t(\zeta_i) + \sum_{j=0}^N D_{ij} \Pi_{j+1/2}, \quad i = 1 : N \quad (59)$$

Note that for the tip enriched scheme, ζ_0 and ζ_{N+1} are located at the actual fracture tips and enrichment with a power-law exponent λ is applied to those finite elements that lie within a radius ρ of the tips. For the scheme with only sign enrichment, ζ_0 and ζ_{N+1} do not correspond to the fracture tips, but rather to the intersection points of the tip line segments and the boundaries of the finite elements containing the tips.

3.2.2. Discretization of the fluid flow equations

By integrating the Reynolds equation (35) over the k th channel element $\Delta\zeta_k$, and using central differencing for the fluxes, we obtain the following equations for $k = 1 : N - 1$:

$$\int_{\zeta_k}^{\zeta_{k+1}} \Omega d\zeta = \left[\Omega^3 \frac{\partial \Pi}{\partial \zeta} \right]_k^{k+1} + \Delta k_0$$

$$\approx \Omega_{k+1}^3 \frac{\Pi_{k+3/2} - \Pi_{k+1/2}}{\zeta_{k+3/2} - \zeta_{k+1/2}} - \Omega_k^3 \frac{\Pi_{k+1/2} - \Pi_{k-1/2}}{\zeta_{k+1/2} - \zeta_{k-1/2}} + \Delta k_0$$

where

$$\Delta k_0 = \begin{cases} 1, & \text{if } 0 \in (\zeta_k, \zeta_{k+1}) \\ \frac{1}{2}, & \text{if } 0 = \zeta_k \text{ or } 0 = \zeta_{k+1} \\ 0, & \text{if } 0 \notin [\zeta_k, \zeta_{k+1}] \end{cases}$$

To approximate the integral $\int_{\zeta_k}^{\zeta_{k+1}} \Omega d\zeta$, we use the backward difference approximation $\Omega \approx \frac{\Omega - \Omega^0}{\Delta\tau}$, where Ω^0 represents the value at the previous time step, and the Trapezoidal rule for evaluation of the integral $\int_{\zeta_k}^{\zeta_{k+1}} \Omega d\zeta$. (Consistent with a backward difference approximation, all variables without a superscript are assumed to be evaluated at the current time-step.) Thus we obtain the following finite volume discretization of the fluid flow equations in the channel:

$$\frac{1}{\Delta\tau} \left(\frac{\Delta\zeta_k}{2} (\Omega_k + \Omega_{k+1}) - \int_{\zeta_k}^{\zeta_{k+1}} \Omega^0 d\zeta \right)$$

$$= \Omega_{k+1}^3 \frac{\Pi_{k+3/2} - \Pi_{k+1/2}}{\zeta_{k+3/2} - \zeta_{k+1/2}} - \Omega_k^3 \frac{\Pi_{k+1/2} - \Pi_{k-1/2}}{\zeta_{k+1/2} - \zeta_{k-1/2}} + \Delta k_0 \quad (60)$$

where $\Delta\zeta_k = \zeta_{k+1} - \zeta_k$ and $k = 1 : N - 1$. The integral $\int_{\zeta_k}^{\zeta_{k+1}} \Omega^0 d\zeta$ is evaluated using the Trapezoidal rule as well, except for those channel elements which at the previous time step were in the tip zone Σ_t , and for which this integral is evaluated using the asymptotic solution (53) for $\Omega^0(\zeta)$.

For the tip elements the finite volume approximation becomes:

$$\int_{-\gamma}^{\zeta_1} \Omega d\zeta \approx \Omega_1^3 \frac{\Pi_{3/2} - \Pi_{1/2}}{\zeta_{3/2} - \zeta_{1/2}} \quad \text{and}$$

$$\int_{\zeta_N}^{\gamma} \Omega d\zeta \approx -\Omega_N^3 \frac{\Pi_{N+1/2} - \Pi_{N-1/2}}{\zeta_{N+1/2} - \zeta_{N-1/2}} \quad (61)$$

Finally, the integrals $\int_{-\gamma}^{\zeta_1} \Omega d\zeta$ and $\int_{\zeta_N}^{\gamma} \Omega d\zeta$ are approximated using backward differencing by evaluating the tip volumes using the asymptotic solution (53) at the current time-step and the previous time-step, taking the difference, and dividing by $\Delta\tau$.

3.2.3. Iterative solution of the coupled equations

For a prescribed time-step $\Delta\tau$ we assume a trial crack length γ at the end of the current time-step and determine the corresponding N -vector of nodal widths $\Omega = (\Omega_1, \dots, \Omega_N)$ and the $(N + 1)$ -vector of pressures $\Pi = (\Pi_{1/2}, \dots, \Pi_{N+1/2})$. These $2N + 1$ unknowns are then determined by solving the $2N + 1$ nonlinear equations comprising the discrete elasticity Eq. (59), which provides N equations, coupled with the discrete Reynolds equation for the channel elements (60), which provides $N - 1$ equations, and the discrete Reynolds equation for the two tip elements (61), which provides a further 2 equations. An initial guess for the nodal quantities is then chosen to be the value at the previous time-step, and the $2N + 1$

nonlinear equations are solved using Newton iteration until a prescribed tolerance is reached.

3.3. Level set strategy for locating the free boundary

In this section we describe a technique that employs an iterative level set approach to locate the unknown fracture front γ at each step of propagation. The algorithm we describe adapts to the XFEM context the implicit level set algorithm (ILSA) that was developed in [16] for modeling propagating hydraulic fractures using the DDM. We will assume that at the m th front iteration, the trial fracture front position $\gamma^{(m)}$ is used as described in Section 3.2 to determine the corresponding vector of nodal widths $\Omega^{(m)}$ and vector of nodal pressures $\Pi^{(m)}$. The trial fracture widths at the nodes closest to the channel-tip boundary, namely $\Omega_2^{(m)}$ and $\Omega_{N-1}^{(m)}$, are used to determine the distance to the closest fracture front by inverting the asymptotic solution for the crack width as a function of distance to the tip. This is used to determine a next iterate $\gamma^{(m+1)}$ for the location of the fracture front. This process is repeated until convergence is achieved, at which stage the tip widths $\Omega_2^{(m+1)}$ and $\Omega_{N-1}^{(m+1)}$ and the location of the fracture front $\gamma^{(m+1)}$ are compatible with the tip asymptote.

3.3.1. Inversion of the tip width asymptote

Consider the crack tip located at $\zeta = \gamma^0$ at time $\tau^0 = \tau - \Delta\tau$ that has moved to an unknown location at $\zeta = \gamma$ at time τ due to the injection of fluid. We assume that the tip width asymptote is known in the functional form (53), that may involve the front velocity $\dot{\gamma}(\tau)$. This form is applicable to the asymptotes (37)–(39); here $\hat{\zeta} = \gamma - \zeta$.

We denote by $\mathcal{T}(\zeta) = -\hat{\zeta}$ the signed distance from a point ζ to the fracture front γ . For points inside the crack, $\mathcal{T}(\zeta) < 0$. The front velocity can be approximated by

$$\dot{\gamma} = -\frac{\mathcal{T}(\zeta) - \mathcal{T}^0(\zeta)}{\Delta\tau} \quad (62)$$

in which \mathcal{T}^0 is the signed distance from point ζ to the front location γ^0 at the previous time, which is known.

The asymptote (53) then becomes

$$\Omega \sim \mathcal{W}\left(-\mathcal{T}; -\frac{\mathcal{T} - \mathcal{T}^0}{\Delta\tau}\right) \quad (63)$$

The above form of the asymptote can then be inverted to yield

$$\mathcal{T}(\zeta) = -\mathcal{W}^{-1}(\Omega(\zeta)) \quad (64)$$

Thus given the value of the crack width Ω at point ζ , the inverse map \mathcal{W}^{-1} provides an estimate of the distance to the fracture front.

Thus, after the crack width Ω and the signed distance \mathcal{T}^0 have been obtained at point ζ , the signed distance $\mathcal{T}(\zeta)$ is found as the root of the nonlinear equation:

$$\Omega - \mathcal{W}\left(-\mathcal{T}; -\frac{\mathcal{T} - \mathcal{T}^0}{\Delta\tau}\right) = 0 \quad (65)$$

and the front is located at

$$\gamma = \zeta - \mathcal{T}(\zeta) \quad (66)$$

For the universal asymptote (37), where the map \mathcal{W} is not known in a closed form, the nonlinear equation (65) has to be solved numerically. For the two limiting regimes (38) and (39), however, it can be solved explicitly following [16]. For example, in the toughness dominated regime (38), \mathcal{T} is found as

$$\mathcal{T}(\zeta) = -\left(\frac{\Omega}{\mathcal{K}}\right)^2$$

The corresponding solution for \mathcal{T} for the viscosity case (39) is provided in detail in [16].

3.3.2. Iterative location of the free boundary

The steps of the iterative algorithm used to generate the results presented in this paper are as follows. At time τ_M , a trial location of the front $\gamma = \gamma^{(m)}$ is chosen. The corresponding vector of nodal widths $\Omega^{(m)}$ and vector of nodal pressures $\Pi^{(m)}$ are obtained using one of the P&W XFEM schemes described in Section 3.2. Then, using the nodal values $\Omega_{N-1}^{(m)}$ and $\mathcal{T}^o(\zeta_{N-1})$, the signed distance \mathcal{T} is found as the root of (65), and the crack front is updated to

$$\gamma^{(m+1)} = \zeta_{N-1} - \mathcal{T} \tag{67}$$

The same technique can be used to determine the location of the fracture front at the other tip. This procedure is repeated until convergence is reached within a predefined tolerance δ_γ ,

$$|\gamma^{(m)} - \gamma^{(m-1)}| < \delta_\gamma \Delta\gamma^{(m-1)} \tag{68}$$

where $\Delta\gamma^{(m)} = \gamma^{(m)} - \gamma^o$ is the estimate of the change in the crack length at iteration m . For the results to be accurate, we must ensure that the node ζ_{N-1} is within the range of validity of the tip width asymptote (53). This is satisfied when the asymptotic validity range spreads over at least two elements from the crack tip. For the P&W XFEM- t scheme the singular crack tip enrichment, and the stiffness matrix of the XFEM, are updated each time the fracture front γ is altered. However, for the P&W XFEM- s scheme the sign enrichment only needs to be updated when the fracture front breaks into a new finite element, which results in substantial savings in computational resources.

4. Numerical results

In the first four examples we present, we consider hydraulic fractures propagating in an infinite homogeneous elastic medium each corresponding to different values of the dimensionless toughness along the MK-edge of parameter space $\mathcal{K} = 0, 1, 2,$ and 3 (see [2]). In all these simulations, we modeled a horizontal crack in a rectangular domain $[-L_x/2, L_x/2] \times [-L_y/2, L_y/2]$ with singly- and doubly-infinite elements of order 9 (see the top part of Fig. 4). In addition, to establish relative independence of the results with

respect to the underlying FE mesh, for the zero toughness case $\mathcal{K} = 0$ we also compare the horizontal crack results to those in which the crack is inclined at 30° to the x -axis (see the bottom part of Fig. 4). In these simulations, the initial solution corresponded to a crack of half-length $\gamma^1 \approx 1$. The crack was propagated until a maximum half-length $\gamma_{max} \approx 3$. This cut-off length was chosen to guarantee that the relative error in the interpolated crack width $\Omega(\zeta, \tau)$ due to approximation of the infinite domain by infinite elements did not exceed 10^{-2} . This roughly corresponded to $\gamma_{max} \approx L_y/2 \approx L_x/4$. The radius of the tip enrichment was kept constant during the simulations and was set to $\rho = 0.25$. The relative tolerance for the fracture front was set to $\delta_\gamma = 10^{-4}$ for the case when $\mathcal{K} = 0$, and to $\delta_\gamma = 10^{-3}$ for the remaining values of \mathcal{K} . For each simulation the following parameters were defined: the domain side lengths L_x and L_y , the mesh size h , the time step $\Delta\tau$, and the power law λ used for the enrichment. We choose the time-scale to be $t_* = 1$. In all simulations in this paper, the Poisson's ratio is set to $\nu = 0.2$, except for the static problem in Section 4.7 in which the crack crosses a bi-material interface.

We compare the results of the simulations to available reference solutions [18,19]. For these comparisons, we define the relative approximation errors in the length, the width, the inlet crack width $\Omega(0, \tau)$, and the inlet pressure $\Pi(0, \tau)$, at each time step as follows:

$$E_\gamma(\tau) = \frac{|\gamma(\tau) - \gamma^{ref}(\tau)|}{\gamma^{ref}(\tau)}, \quad E_\Omega(\tau) = \sqrt{\frac{\sum_{i=1}^N (\Omega_i - \Omega_i^{ref})^2}{\sum_{i=1}^N (\Omega_i^{ref})^2}}$$

$$E_{\Omega(0)}(\tau) = \frac{|\Omega(0, \tau) - \Omega^{ref}(0, \tau)|}{\Omega^{ref}(0, \tau)},$$

$$E_{\Pi(0)}(\tau) = \frac{|\Pi(0, \tau) - \Pi^{ref}(0, \tau)|}{\Pi^{ref}(0, \tau)} \tag{69}$$

where the superscript ref denotes the quantities corresponding to the reference solution at time τ . Note that the above definition of the width error $E_\Omega(\tau)$, based on the nodal crack widths, can be viewed as a discrete version of the L_2 -norm of the error, scaled by the L_2 -norm of the reference solution:

$$E_\Omega(\tau) \sim \frac{\|\Omega - \Omega^{ref}\|_{L_2(-\gamma, \gamma)}}{\|\Omega^{ref}\|_{L_2(-\gamma, \gamma)}} \tag{70}$$

In the second sequence of examples presented in Section 4.6, we study the convergence of both XFEM schemes with respect to the finite element mesh size h . Finally, in Section 4.7 we present results for a hydraulic fracture propagating in the viscous regime through a bi-material interface.

4.1. Performance of XFEM- t and XFEM- s for a static BVP ($\mathcal{K} = 0$ and 3)

To understand the behavior of the XFEM- t and XFEM- s schemes, we first compare their accuracy for a mixed boundary value problem (BVP) in which the crack in the infinite elastic medium is subjected to a given pressure Π_c in the channel and a given crack width Ω_t within the tip region:

$$\sigma_n^+ = \sigma_n^- = -\Pi_c(\zeta) \quad \text{for } \zeta \in \Sigma_c, \quad \sigma_s^+ = \sigma_s^- = 0 \quad \text{for } \zeta \in \Sigma$$

$$[[\mathbf{u}]]_\Sigma \cdot \mathbf{n} = \Omega_t(\zeta) \quad \text{for } \zeta \in \Sigma_t$$

It is precisely this BVP which the XFEM component of the algorithm solves repeatedly during the HF propagation process so, for this test, the configuration of the crack in the computational domain and the boundary conditions are chosen to correspond to a typical situation for a propagating HF. In particular, given the pressure Π_c and width Ω_t associated with either the M-vertex solution ($\mathcal{K} = 0$) or the

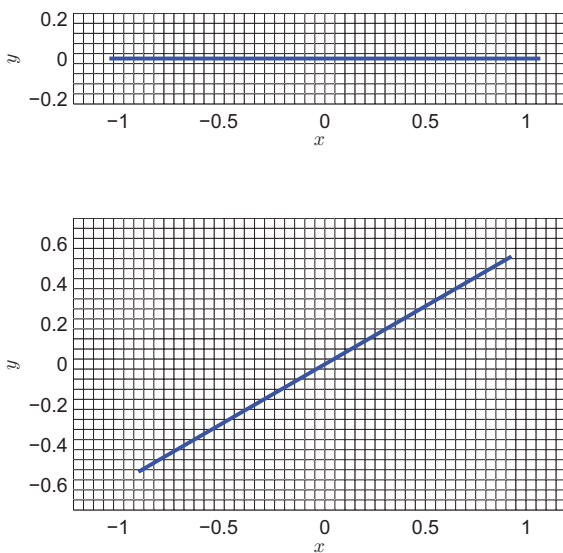


Fig. 4. Fragments of the FEM mesh and the crack configuration at the first step of propagation in simulations corresponding to $\mathcal{K} = 0$, with a horizontal crack (top) or an inclined crack (bottom).

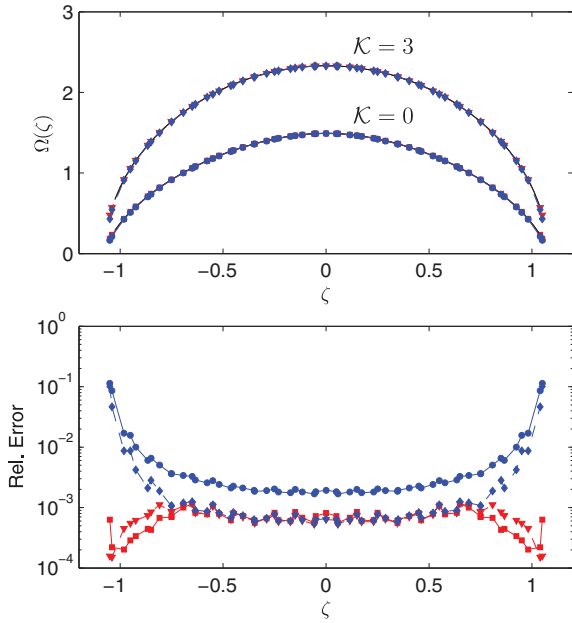


Fig. 5. Simulation results for a static mixed BVP for an inclined crack: crack width (top) and relative error $E_{\Omega(\zeta)}$ (bottom). Results correspond to: $\kappa = 0$ (solid red with squares for XFEM-t, solid blue with circles for XFEM-s) and $\kappa = 3$ (dashed red with triangles for XFEM-t, dashed blue with diamonds for XFEM-s). The reference solution $\Omega^{ref}(\zeta)$ is shown in solid black (top). (For interpretation of the references to color in this figure legend, the reader is referred to the web version of this article.)

MK-edge solution ($\kappa = 3$) determine the corresponding channel width Ω_c . The power law used for the tip enrichment is $\lambda = 2/3$ for $\kappa = 0$ and $\lambda = 1/2$ for $\kappa = 3$. The crack is inclined at 30° to the x -axis as shown in the lower part of Fig. 4. The problem was solved for $L_x = 12$, $L_y = 6.05$, $h = 0.05$, using infinite elements of order 9. The crack's half-length is $\gamma = 1.075$, and the radius of the tip enrichment is set to $\rho = 0.25$.

The crack widths $\Omega_i = \Omega(\zeta_i)$ are computed at the nodes ζ_i using the XFEM-t and XFEM-s. These results are compared to the reference solution $\Omega^{ref}(\zeta)$ (M-vertex solution for $\kappa = 0$, MK-edge solution for $\kappa = 3$) in Fig. 5. The relative error for these results is computed according to:

$$E_{\Omega(\zeta)} = \frac{|\Omega(\zeta) - \Omega^{ref}(\zeta)|}{\Omega^{ref}(\zeta)}$$

Several observations can be made from this comparison. As would be expected, the results of XFEM-t are closer to the reference solutions within the radius of enrichment $\rho = 0.25$ from each crack tip. However, the errors in the solutions from XFEM-t and XFEM-s are roughly of the same order farther from the crack tips, where each scheme uses only the sign enrichment to represent the displacement jump. The major influence of the tip enrichment is localized to the tip-enriched zone.

4.2. HF propagation in a viscous regime ($\kappa = 0$)

We first consider an HF propagating on the M-vertex for which the toughness is $\kappa = 0$. The XFEM solutions are compared to the M-vertex analytic solution [18,19], which is also used to generate initial solutions for the simulations. The propagation condition for this problem corresponds to the viscous width asymptote (39), for which the power-law exponent for the singular tip enrichment must be set to $\lambda = 2/3$. The P&W XFEM-t scheme with $\lambda = 2/3$ enrichment and the P&W XFEM-s scheme were used to solve the

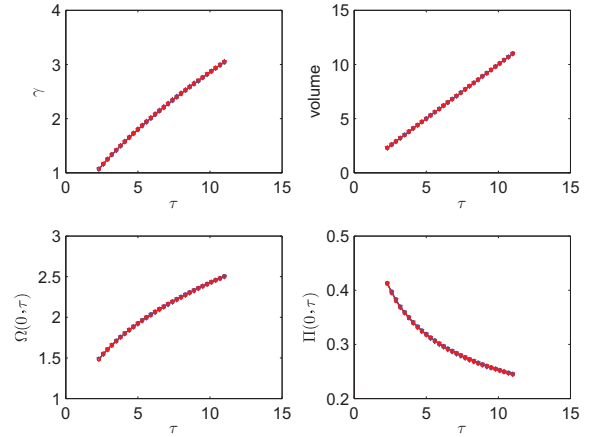


Fig. 6. Simulation results for $\kappa = 0$: evolution of: the crack half-length γ , the fluid volume $\int_{-\gamma}^{\gamma} \Omega d\zeta$, the inlet crack width $\Omega(0, \tau)$, and the inlet pressure $\Pi(0, \tau)$. Results correspond to: the horizontal crack (solid red with squares for XFEM-t, solid blue with circles for XFEM-s), the inclined crack (dashed red with triangles for XFEM-t, dashed blue with diamonds for XFEM-s), and the reference solution (solid black). (For interpretation of the references to color in this figure legend, the reader is referred to the web version of this article.)

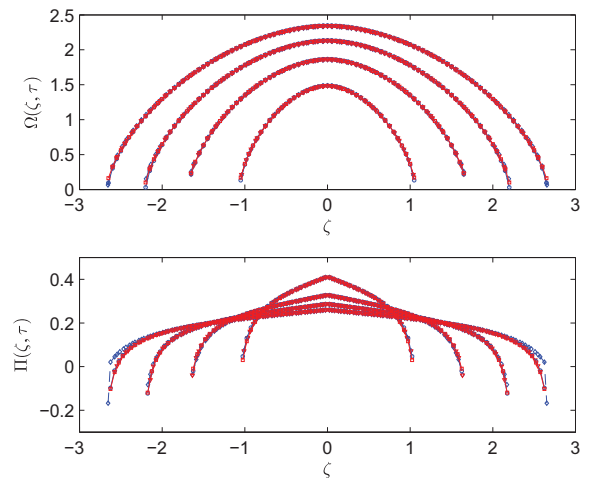


Fig. 7. Simulation results for $\kappa = 0$: the crack width and the pressure at times $\tau = 2.30 + 2.25(k - 1)$, with $k = 1, \dots, 4$. Results correspond to: the horizontal crack (solid red with squares for XFEM-t, solid blue with circles for XFEM-s), the inclined crack (dashed red with triangles for XFEM-t, dashed blue with diamonds for XFEM-s), and the reference solution (solid black). (For interpretation of the references to color in this figure legend, the reader is referred to the web version of this article.)

coupled equations. Both these schemes used the level set approach to locate the fracture front by means of the tip asymptote (39).

The simulation was performed for $L_x = 12$, $L_y = 6.05$, $h = 0.05$, and assuming a constant time-step $\Delta\tau = 0.15$. For the horizontally oriented crack, with one element in each tip region, five to eight level set iterations within each time-step were typically required to reach convergence to the fracture front. For the crack inclined at 30° to the x -axis, the number of iterations per time-step varied between five and twenty-five. In this case the number of elements n in each tip region was allowed to vary between 1 and 3 to ensure that the length of each of the two tip regions was not smaller than $h/5$. The results are compared to the M-vertex solution in Figs. 6–8.

Fig. 6 shows the evolution with time of the crack half-length γ , the fluid volume $\int_{-\gamma}^{\gamma} \Omega d\zeta$, the inlet crack width $\Omega(0, \tau)$, and the inlet pressure $\Pi(0, \tau)$. A few snapshots of the nodal crack widths and the nodal pressures are shown in Fig. 7. On this scale all the solutions

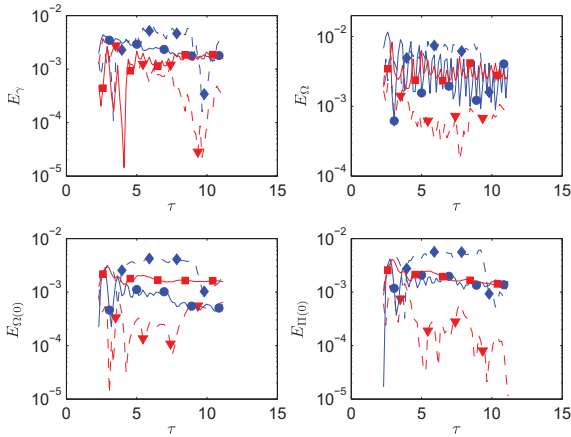


Fig. 8. Relative errors for $\mathcal{K} = 0$ in: the length, the width, the inlet width and the inlet pressure. Results correspond to: the horizontal crack (solid red with squares for *XFEM-t*, solid blue with circles for *XFEM-s*), the inclined crack (dashed red with triangles for *XFEM-t*, dashed blue with diamonds for *XFEM-s*). (For interpretation of the references to color in this figure legend, the reader is referred to the web version of this article.)

were virtually indistinguishable from the M-vertex solution. To investigate the errors more closely, we plot the relative approximation errors in length and width, $E_\gamma(\tau)$ and $E_\Omega(\tau)$, as well as in the inlet width and inlet pressure, $E_{\Omega(0)}(\tau)$ and $E_{\Pi(0)}(\tau)$ in Fig. 8. It can be seen that for the horizontal crack, the errors for the *XFEM-t* solution and for the *XFEM-s* solution ultimately asymptote to roughly the same order, less than one percent of the solution, and do not grow with time. Both these schemes exhibit oscillations in their errors that are caused by the variations in the tip locations within the elements of the underlying FE mesh. The *XFEM-s* naturally exhibits larger error oscillations due to the fact that the tip is treated in a weak sense and because the sign enrichment is updated less frequently. It is possible that the *XFEM-t* and *XFEM-s* schemes have relative errors that are of a similar order when they approach the level of accuracy of the reference solution as it will be discussed in Section 4.6.

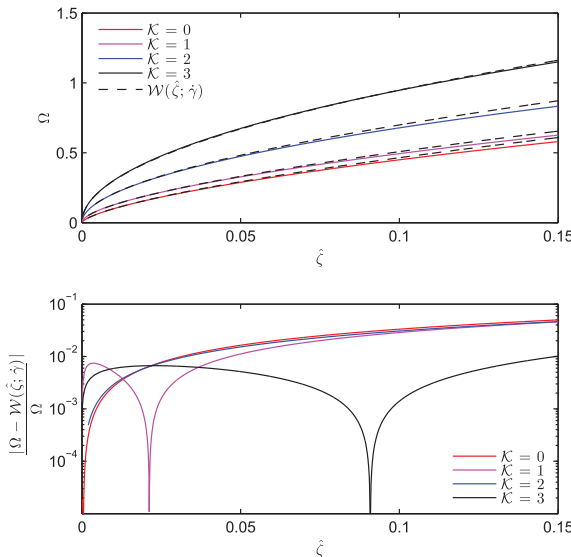


Fig. 9. Range of validity of the tip width asymptote (53) (viscosity asymptote for $\mathcal{K} = 0$, universal asymptote for $\mathcal{K} = 1, 2$, and toughness asymptote for $\mathcal{K} = 3$). The results correspond to the reference solutions (M-vertex for $\mathcal{K} = 0$, MK-edge for $\mathcal{K} = 1, 2, 3$) for a crack of a unit half-length $\gamma = 1$.

For the case in which the crack is inclined relative to the underlying FE mesh, the errors for the *XFEM-t* are smaller than those of *XFEM-s* by about an order of magnitude. In addition, the errors of the inclined *XFEM-t* solution with $n = 1$ to 3 tip elements are consistently lower than those for the aligned *XFEM-t* solution which only has a single element in each tip region. However, for the *XFEM-s* solution, the errors for the inclined crack with $n = 1$ to 3 tip elements are not better than those from aligned *XFEM-s*. This suggests that, in order to make use of the advantages of the tip enrichment, a larger tip zone Σ_t should be used, over which the asymptotic width constraint (57) is applied in the mixed BVP.

Fig. 9 shows a comparison of the crack width Ω corresponding to the reference solutions with the appropriate tip asymptotes for $\mathcal{K} = 0, 1, 2$, and 3. In the *XFEM* simulations for $\mathcal{K} = 0$ the viscosity asymptote (39) was applied for $\hat{\xi}/\gamma$ typically less than 8%. In this range, the accuracy of the asymptote (39) for the M-vertex solution is of the order 10^{-2} , as shown in Fig. 9. The order of errors E_γ , E_Ω , $E_{\Omega(0)}$ and $E_{\Pi(0)}$ is therefore consistent with the accuracy level of the tip asymptote used to prescribe the tip width in the mixed BVP and to locate the fracture front in the numerical model.

Due to the constraint on γ_{max} , the error due to the infinite domain approximation does not exceed 10^{-2} . The fact that the errors shown in Fig. 8 do not grow as the crack tip approaches the finite-infinite element boundary provides further evidence that these errors are not related to the approximation due to the infinite elements.

4.3. Viscosity-toughness transition regime ($\mathcal{K} = 1$)

We now consider the case with $\mathcal{K} = 1$, which corresponds to the viscosity-toughness transition. We use the MK-edge solution with $\mathcal{K} = 1$ as a reference solution. The tip enrichment used by the *XFEM-t* scheme assumes $\lambda = 2/3$. The universal tip asymptote (37) is used by the level set algorithm in both *XFEM* solutions to locate the fracture front and to set the tip widths. This asymptote is applied within 1–7% of the fracture length from the fracture tip. Fig. 9 shows that within this range the universal asymptote can approximate the tip width in this problem with an accuracy of roughly 10^{-2} .

We ran the ILSA-*XFEM* schemes for $L_x = 12$, $L_y = 6.04$, $h = 0.04$, and $\Delta\tau = 0.1$. The typical number of front iterations required for convergence to the fracture front were 4–6. The results for both schemes show close agreement with the reference MK-edge

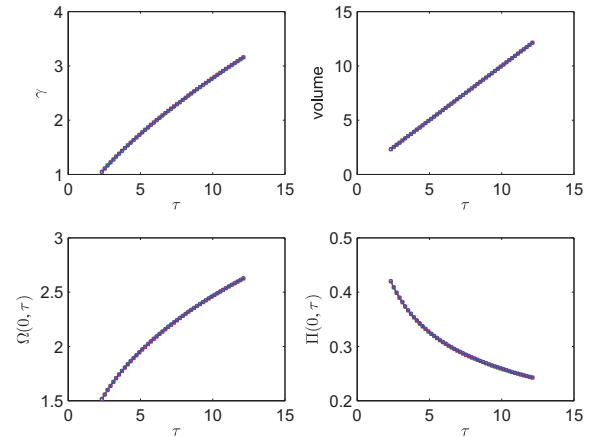


Fig. 10. Simulation results for $\mathcal{K} = 1$: evolution of the crack half-length γ , the fluid volume $\int_{\Omega} \Omega d\zeta$, the inlet crack width $\Omega(0, \tau)$, and the inlet pressure $\Pi(0, \tau)$. Results correspond to: *XFEM-t* (solid red with squares), *XFEM-s* (solid blue with circles), and the reference solution (solid black). (For interpretation of the references to color in this figure legend, the reader is referred to the web version of this article.)

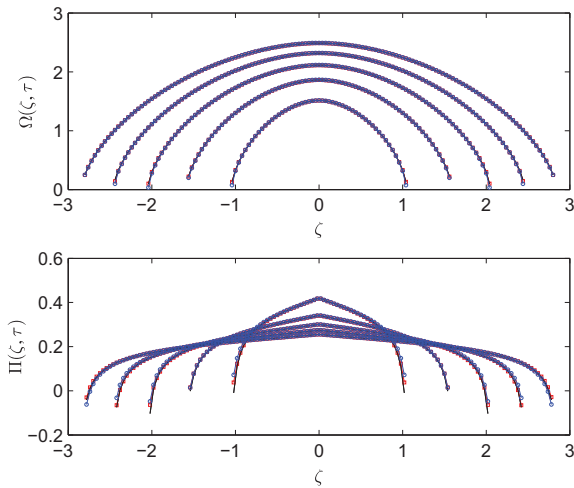


Fig. 11. Simulation results for $\kappa = 1$: crack width and pressure at times $\tau = 2.33 + 2(k - 1)$, with $k = 1, \dots, 5$. Results correspond to: *XFEM-t* (solid red with squares), *XFEM-s* (solid blue with circles), and the reference solution (solid black). (For interpretation of the references to color in this figure legend, the reader is referred to the web version of this article.)

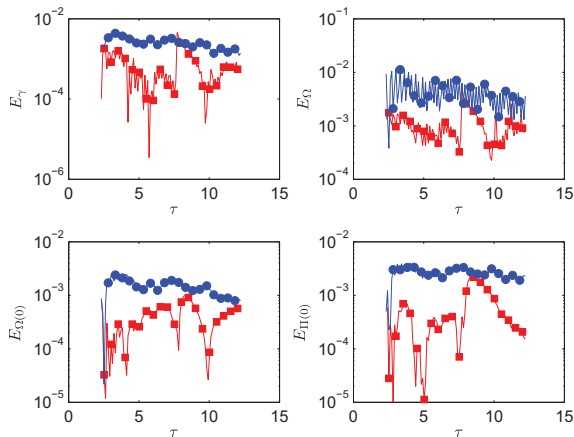


Fig. 12. Relative errors for $\kappa = 1$ in: the length, the width, the inlet width and the inlet pressure. Results correspond to: *XFEM-t* (solid red with squares) and *XFEM-s* (solid blue with circles). (For interpretation of the references to color in this figure legend, the reader is referred to the web version of this article.)

solution (see Figs. 10–12). The relative errors asymptote at around 10^{-3} for *XFEM-t* and lower than 10^{-2} for *XFEM-s*, and do not increase with time. The relative errors are smaller for the *XFEM-t* scheme, however, the *XFEM-s* scheme provides stable results within 1%.

4.4. Beyond the viscosity-toughness transition regime ($\kappa = 2$)

We now consider the case $\kappa = 2$, which is just beyond the viscosity-toughness transition. We use the MK-edge solution with $\kappa = 2$ as a reference solution, and choose $\lambda = 1/2$ as the power-law exponent for the singular tip enrichment. We ran the simulations for the same discretization level as in the previous example with $\kappa = 1$ (that is, $L_x = 12$, $L_y = 6.04$, $h = 0.04$, and $\Delta\tau = 0.1$). Again, the universal asymptote (37) was used to locate the fracture front by the level set algorithm and to provide the boundary condition for the crack tip width in the mixed BVP, within 1–7% of the fracture length from the tip. Fig. 9 shows that within this distance from the fracture tip, the universal asymptote can approximate the tip width for $\kappa = 2$ with a relative accuracy of roughly 10^{-2} .

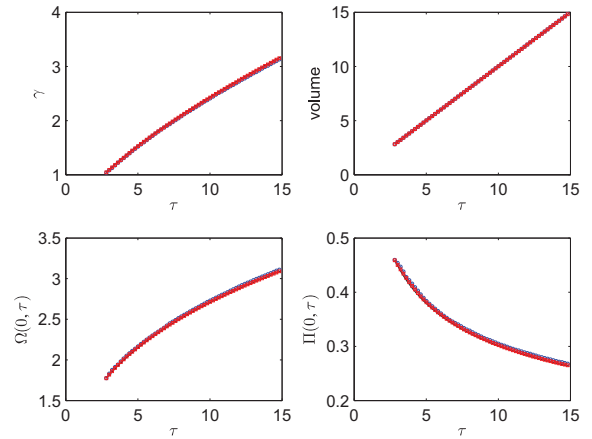


Fig. 13. Simulation results for $\kappa = 2$: evolution of the crack half-length γ , the fluid volume $\int_{\Omega} \Omega d\xi$, the inlet crack width $\Omega(0, \tau)$, and the inlet pressure $\Pi(0, \tau)$. Results correspond to: *XFEM-t* (solid red with squares), *XFEM-s* (solid blue with circles), and the reference solution (solid black). (For interpretation of the references to color in this figure legend, the reader is referred to the web version of this article.)

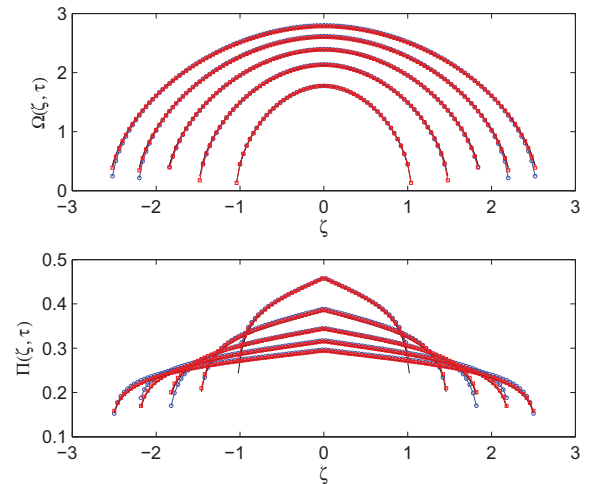


Fig. 14. Simulation results for $\kappa = 2$: the crack width and pressure at times $\tau = 2.82 + 2(k - 1)$, with $k = 1, \dots, 5$. Results correspond to: *XFEM-t* (solid red with squares), *XFEM-s* (solid blue with circles), and the reference solution (solid black). (For interpretation of the references to color in this figure legend, the reader is referred to the web version of this article.)

The results show close agreement with the reference solution, as can be seen from Figs. 13–15. The relative errors asymptote at around 10^{-2} for the *XFEM-s* and lower for the *XFEM-t* and do not increase with time (Fig. 15). As in the previous example, the results of the *XFEM-t* are better than those from the *XFEM-s*, however, the *XFEM-s* scheme still provides stable results having an error of 2% or lower. It can be seen that, for the same level of discretization, the approximation errors for $\kappa = 1$ asymptote at lower levels, than for $\kappa = 2$. This observation is consistent with Fig. 9, which shows that within the distance 1–7% of the fracture length from the fracture tip, where the universal asymptote was applied in the simulations, the asymptote for $\kappa = 1$ provides a more accurate approximation than that for $\kappa = 2$.

The typical number of front iterations required to converge to the fracture front in this example was 8–10 for the *XFEM-t* scheme and was less than 20 for *XFEM-s* scheme. We observe from this and from the following example with $\kappa = 3$, the tendency of convergence rate for the front iterations to deteriorate with increasing toughness κ .

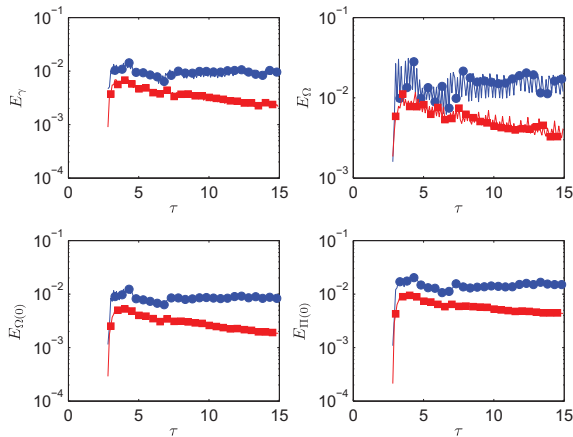


Fig. 15. Relative errors for $\mathcal{K} = 2$ in: the length, the width, the inlet width and the inlet pressure. Results correspond to: *XFEM-t* (solid red with squares) and *XFEM-s* (solid blue with circles). (For interpretation of the references to color in this figure legend, the reader is referred to the web version of this article.)

4.5. HF propagation in a toughness dominated regime ($\mathcal{K} = 3$)

Finally we consider a large toughness case for which $\mathcal{K} = 3$. The reference solution for this problem is given by the MK-edge solution. The toughness tip asymptote (38) is used in the level set approach to locate the front, and the power-law exponent for the singular enrichment is set to $\lambda = 1/2$. Fig. 9 shows that the toughness asymptote approximates the tip width in this case with less than 10^{-2} relative error within 15% of the crack length from the tip. This large region of validity of the tip asymptote makes it possible to apply the level set logic further from the fracture tip, which enables one to use less elements for the fracture discretization. However, the non monotonic behavior of this asymptote, which can be seen in Fig. 9, implies that the error will not necessarily decrease as the tip region relative to the crack length decreases. Indeed, one cannot guarantee a relative error level less than 5×10^{-3} when using this asymptote. Because of this observation, the simulation was performed for $L_x = 12$, $L_y = 6.06$, and $h = 0.06$. The asymptote (38) was typically applied within 2–11% of the fracture length from the fracture tip.

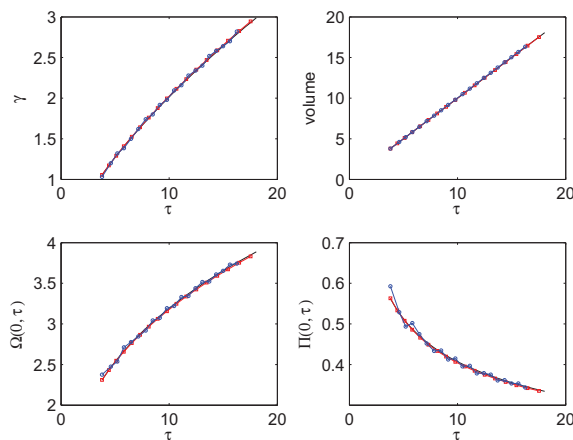


Fig. 16. Simulation results for $\mathcal{K} = 3$: evolution of the crack half-length γ , the fluid volume $\int_{-\gamma}^{\gamma} \Omega d\zeta$, the inlet crack width $\Omega(0, \tau)$, and the inlet pressure $\Pi(0, \tau)$. Results correspond to: *XFEM-t* (solid red with squares), *XFEM-s* (solid blue with circles), and the reference solution (solid black). (For interpretation of the references to color in this figure legend, the reader is referred to the web version of this article.)

It was found that it was necessary to use a relatively large time-step $\Delta\tau$ for *XFEM-s* to achieve convergence. Stair-casing can occur in the *XFEM-s* fracture length solution if the time-step is too small to advance the fracture tips significantly. Similar stair-casing behavior has also been observed in ILSA-DDM schemes if the time-step is so small that the front advance can stagnate. For this experiment we used the following simple adaptive time-stepping scheme: the time-step was chosen so that the expected crack front advance was approximately equal to one element size h , that is $\Delta\tau = h/\dot{\gamma}$ where $\dot{\gamma}$ is the crack front velocity at the previous time-step.

The number of front iterations required for convergence to the fracture front typically exceeded 20 for the *XFEM-t* and was typically between 8 and 30 for the *XFEM-s*, which is considerably larger than that for $\mathcal{K} = 0$ and 1. This supports the tendency, observed in the previous three examples, that as \mathcal{K} increases the rate of convergence of the fracture front iterations deteriorates.

The results of the *XFEM* schemes agree well with the MK-edge solution, as shown in Figs. 16–18. The relative errors for both schemes do not increase with time and asymptote to roughly the same order (see Fig. 18). The fact that both schemes are limited to errors that are larger than 5×10^{-3} is consistent with the accuracy limitations of the $\mathcal{K} = 3$ tip asymptote mentioned above. In Fig. 17 the fracture widths and pressures at selected time steps are compared with the MK-edge solution. Since the two *XFEM* schemes use different time-steps the solutions are sampled at different times. However, each numerical solution is compared to the reference solution at the corresponding time horizon. Except for the initial pressure, in which there is a noticeable difference in the *XFEM-s* solution, all the other solutions show close agreement with the corresponding reference solutions. These initial errors in the *XFEM-s* solutions can also be seen at earlier times, but these oscillations reduce to less than 1%.

4.6. Convergence with respect to the finite element mesh size

Convergence of the *XFEM-t* and *XFEM-s* schemes with respect to the finite element mesh size h has been investigated in [17] for a static elastic mixed BVP with given displacement along the outer boundary Γ , given tractions along the channel part of the crack Σ_c , and a prescribed power-law crack width $\Omega_t \sim \zeta^2$ in the tip zone

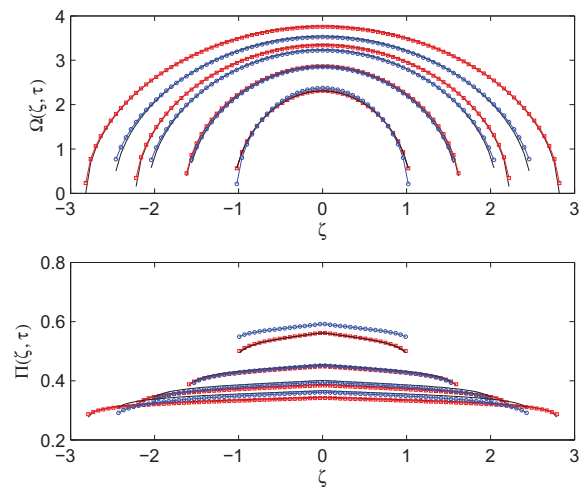


Fig. 17. Simulation results for $\mathcal{K} = 3$: the crack width and pressure at times $\tau = 3.79, 7.32, 11.58, 16.48$ for *XFEM-t* and at times $\tau = 3.79, 7.15, 10.45, 13.71$ for *XFEM-s*. Results correspond to: *XFEM-t* (solid red with squares), *XFEM-s* (solid blue with circles), and the reference solution (solid black). (For interpretation of the references to color in this figure legend, the reader is referred to the web version of this article.)

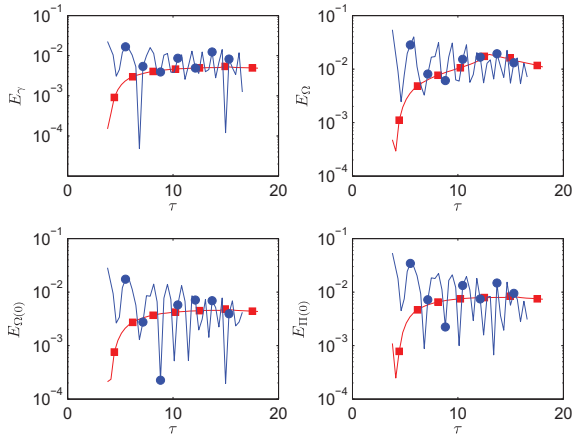


Fig. 18. Relative errors for $\mathcal{K} = 3$ in: the length, the width, the inlet width and the inlet pressure. Results correspond to: *XFEM-t* (solid red with squares) and *XFEM-s* (solid blue with circles). (For interpretation of the references to color in this figure legend, the reader is referred to the web version of this article.)

Σ_t , with $1/2 \leq \lambda < 1$. These numerical experiments show that the approximation error in the crack width within the channel Σ_c in the *XFEM-t* solution decays according to

$$\|\Omega - \Omega^{ref}\|_{L_2(\Sigma_c)} \sim O(h^2) \tag{71}$$

and in the *XFEM-s* solution according to

$$\|\Omega - \Omega^{ref}\|_{L_2(\Sigma_c)} \sim O(h) \tag{72}$$

Here, $L_2(\Sigma_c)$ is the integral L_2 norm over the channel.

To study the convergence of the *XFEM-t* and *XFEM-s* schemes for a propagating hydraulic fracture, we performed simulations for $\mathcal{K} = 0$ with several finite element mesh refinements. To have an identical computational domain in each simulation, we used a square domain $[-L_x/2, L_x/2] \times [-L_y/2, L_y/2]$ of size $L_x = L_y = 7.2$, discretized into $N_x \times N_x$ square finite elements with side length $h = L_x/N_x$, in which an odd number N_x varied between 47 and 171 for the *XFEM-t* scheme, and between 47 and 221 for the *XFEM-s* scheme. Infinite elements of order 9 were used. The fluid source was located at the origin $x = y = 0$. The initial horizontal crack of half-length $\gamma^1 = 1$ was propagated for 20 steps assuming a constant time-step $\Delta\tau = 0.15$. The viscous tip asymptote (39) was used by the level set algorithm to locate the fracture front and to set the tip widths. In the *XFEM-t* scheme the radius of the tip enrichment region was set to $\rho = 0.25$ and the power-law exponent for the singular tip enrichment was set to $\lambda = 2/3$. The relative tolerance for the location of the fracture front was set to $\delta_\gamma = 10^{-4}$. To avoid the instabilities associated with extremely small elements along the crack that can result from an awkward intersection of the crack with the underlying FEM mesh, we ensured that the size of the tip region Σ_t at each crack tip was no smaller than $0.01 \times h$ for the *XFEM-t* scheme and up to $h/5$ for the *XFEM-s* scheme; one tip element at each crack tip was typically sufficient for most of the time-steps.

The results were compared with the reference semi-analytical M-vertex solution [18,19]. The convergence plots for the error in the crack length, $E_\gamma(\tau)$, and the error in the crack width, $E_\Omega(\tau)$, are shown in Fig. 19. To account for the fact that the XFEM solutions settle over the first few steps, the errors $E_\gamma(\tau)$ and $E_\Omega(\tau)$ shown in Fig. 19 were averaged over steps 5–20.

In the log–log plots shown in Fig. 19, the errors initially decay linearly and then stagnate over the last three mesh refinements. The same was observed in the behavior of the averaged errors in

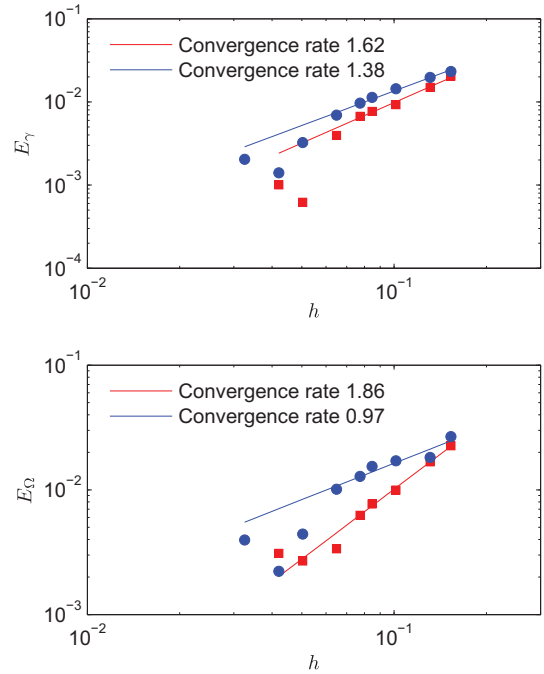


Fig. 19. Convergence of the average relative errors in the length and the width. Results correspond to: *XFEM-t* (solid red with squares) and *XFEM-s* (solid blue with circles). (For interpretation of the references to color in this figure legend, the reader is referred to the web version of this article.)

the inlet width and inlet pressure, $E_{\Omega(0)}$ and $E_{I(0)}$. There are two possible explanations for this phenomenon. Firstly, the errors will stagnate if the approximation error due to the infinite elements becomes significant compared to the other approximation errors in the coupled XFEM schemes. Secondly, such a stagnation in the errors will also occur if the error in the reference semi-analytical solution [18] exceeds the error in the XFEM schemes at such a fine mesh. This reference solution is available in the form of a series expansion in which the series coefficients are found numerically. The relative error in this solution (based on 10 terms in the series) is of the order 10^{-3} – 10^{-4} [18]. There is similar evidence of such errors in the reference solution [18] reported in [24]. It is thus only meaningful to use this reference solution for the convergence study while the XFEM results differ from this solution by about 10^{-3} or more. This stagnation effect can also be seen in the numerical results presented in Sections 4.2, 4.3, 4.4 and 4.5. For example, for the error plots for the case $\mathcal{K} = 0$ shown in Fig. 8, the *XFEM-t* and *XFEM-s* schemes have relative errors that are of a similar order when they approach the level of accuracy of the 10-term reference solution, which is of the order 10^{-3} – 10^{-4} . However, for the case $\mathcal{K} = 2$ shown in Fig. 15, the *XFEM-t* scheme is clearly superior to the *XFEM-s* scheme. The difference, in this case is that the reference solution uses a 30-term series approximation for which the error level is of the order 10^{-4} – 10^{-5} .

For this reason we only sample the convergence rates for results that fall within the range of linear decay of the logarithms of the errors. Thus the rates shown in Fig. 19 were computed by excluding the last three mesh refinements for each XFEM scheme.

As expected, the results converge faster for the *XFEM-t* scheme than for the *XFEM-s* scheme. In particular, the convergence rate for the width error E_Ω in Fig. 19 is approximately quadratic for the *XFEM-t* scheme and linear for the *XFEM-s* scheme. As mentioned before (70), E_Ω is roughly equivalent to the scaled L_2 -norm of the

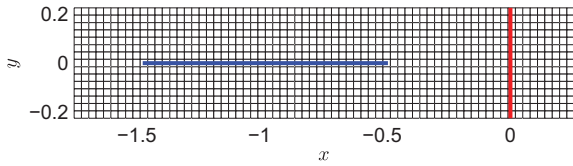


Fig. 20. Fragment of the FEM mesh and the initial crack configuration in the simulation with bi-material interface crossing. The crack is depicted by the blue line; the interface is depicted by the red line. Material I is to the left of the interface. (For interpretation of the references to color in this figure legend, the reader is referred to the web version of this article.)

error in the crack width. These results are therefore consistent with the estimates (71) and (72) for the related static mixed BVP.

4.7. Propagation of a hydraulic fracture through a bi-material interface

To show the potential of the proposed coupled XFEM schemes for modeling propagating hydraulic fractures in non-homogeneous materials, we simulate a situation in which a fracture is crossing a bi-material interface. For this purpose, we assume that the crack tips propagate according to the viscous tip asymptote (39), applicable for the case when most of the energy is dissipated by driving the viscous fluid through the fracture compared to the energy required to break the rock. We choose not to investigate the case of a hydraulic fracture propagating through the bi-material interface in the toughness dominated regime as this would require an asymptotic solution that constantly changes as the crack tip approaches the interface. This, far more complex situation, is still an open question that needs to be resolved by detailed asymptotic analysis and is beyond the scope of this paper.

The two materials are assumed to have contrasting Young's moduli such that $E_2 < E_1$, where the material to the left (right) of the interface has a Young's modulus E_1 (E_2) (see Fig. 20); the rest of the material properties are identical. The fracture is assumed

to propagate initially within material I and orthogonal to the interface. The materials are assumed to be perfectly bonded, so that the hydraulic fracture propagates through the interface without material debonding along the interface.

Due to the bi-material interface the fracture does not grow symmetrically. The only modification to the formulation presented above to accommodate this situation is for the left crack tip located at $\zeta = -\gamma_L$ with respect to the source and the right crack tip located at $\zeta = \gamma_R$ to be able to grow independently. The level-set algorithm is used to locate the position of each crack tip independently according to the M-vertex tip asymptote.

Before embarking on the dynamic crack experiments in the bi-material medium, we tested the XFEM-s scheme with infinite elements for a static elastic BVP in which a crack crosses a bi-material interface and for which reference solutions have been provided by Erdogan and Biricikoglu using a singular integral equation approach [31] and Peirce and Siebrits using a uniform asymptotic solution for a displacement discontinuity in a layered elastic medium [32]. In this problem, the crack faces are subject to a given pressure. Since the XFEM-s is based on using mixed boundary conditions along the crack, we used the given pressure only within the channel Σ_c , while within the tip region Σ_t we specified the crack width according to the solution from [32]. As can be seen from Fig. 21 the resulting crack width in the channel region Σ_c computed using 84 elements for $b_2/b_1 = 0.05$ and 90 elements for $b_2/b_1 = 1, 2$ by the XFEM-s scheme is in good agreement with the solution provided by Erdogan and Biricikoglu [31] and virtually indistinguishable from the high resolution uniform displacement discontinuity (DD) solution provided by Peirce and Siebrits [32] in which 840, 1600 and 2400 elements were used, respectively, for $b_2/b_1 = 0.05, 1, 2$. Indeed, the only solution for which there is a noticeable difference is the small penetration case, in which $b_2/b_1 = 0.05$. Because of the stretched coordinate, these results are quite deceptive. The XFEM solution only uses 4 elements to represent that part of the crack that has penetrated into region II.

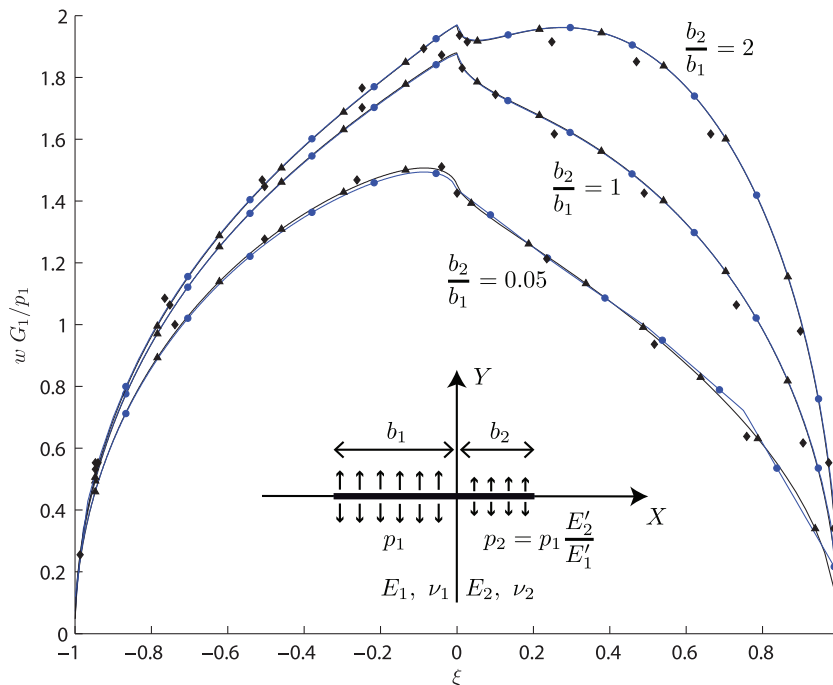


Fig. 21. Crack width for a static crack crossing a bi-material interface. The crack is subject to a uniform pressure p_1 within material I with $E_1 = 10^7$ psi, $\nu_1 = 0.3$, and a uniform pressure p_2 within material II with $E_2 = 4.45 \times 10^5$ psi, $\nu_2 = 0.35$. Results correspond to: [31] (black diamonds), [32] (solid black lines with triangles), and XFEM-s (solid blue lines with circles). The scaled coordinate along the crack is defined by $\xi = X/b_1$ for $X \leq 0$ and $\xi = X/b_2$ for $X > 0$. The crack width is scaled by p_1/G_1 in which $G_1 = E_1/(2(1 + \nu_1))$. (For interpretation of the references to color in this figure legend, the reader is referred to the web version of this article.)

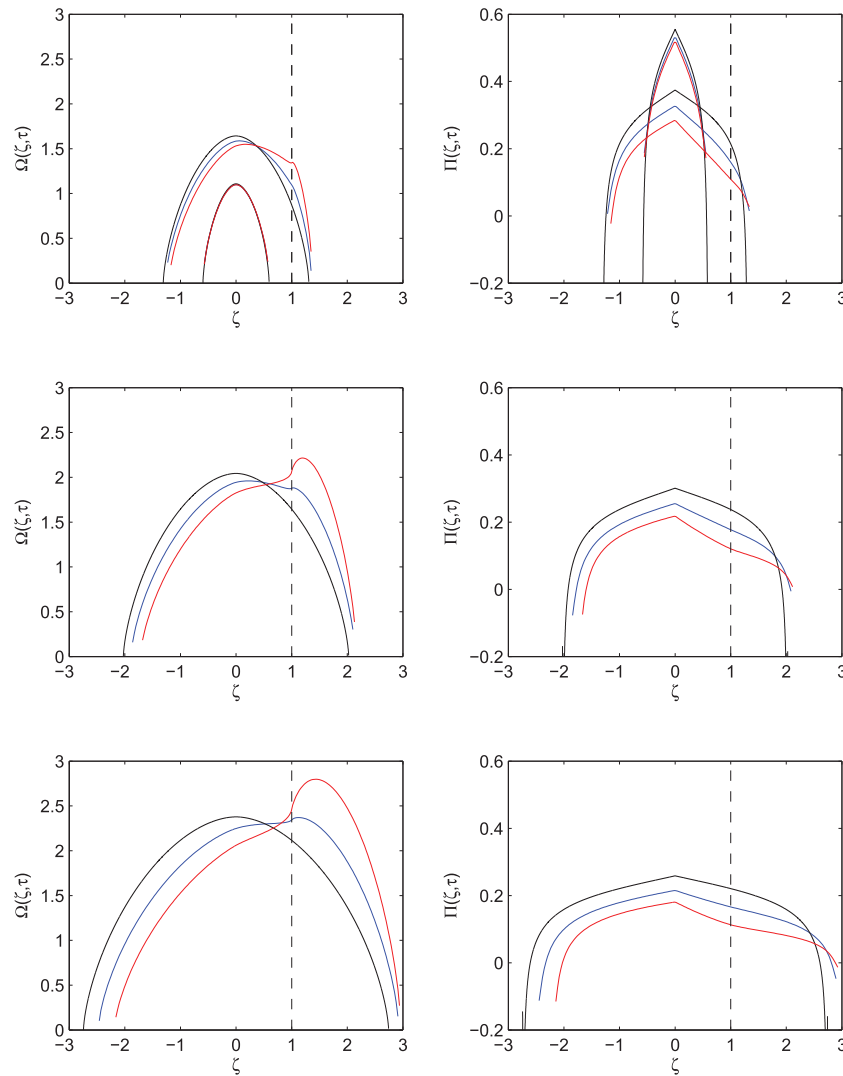


Fig. 22. Simulation results obtained by *XFEM-s* for a hydraulic fracture crossing a bi-material interface: the crack width and pressure at times $\tau = 0.95$ and 3.10 (top), $\tau = 5.97$ (middle), and $\tau = 9.42$ (bottom). Results correspond to: $E_2/E_1 = 0.2$ (solid red), $E_2/E_1 = 0.5$ (solid blue), and the M-vertex solution [18] with $E_2/E_1 = 1$ (solid black). Dashed black line depicts the location of the interface. (For interpretation of the references to color in this figure legend, the reader is referred to the web version of this article.)

The *XFEM-s* solution enforces the correct volume in this tip element in a weak sense according to the variational principle given in (43). Within the tip element the *XFEM-s* solution is represented by the appropriate linear approximation that has the same volume as the prescribed asymptotic solution. The close agreement between the *XFEM* solution and the uniform DD solution, which use completely different approximation schemes, indicates that the results in [32] provide more accurate reference solutions than those given in [31].

The propagation was modeled by the *XFEM-s* scheme for the two cases: $E_2/E_1 = 0.5$ and $E_2/E_1 = 0.2$. The Poisson's ratio for each material is set to $\nu = 0.2$. In both cases, in order to present the results in a dimensionless form, the scaling factor $E' = E_1/(1 - \nu^2)$ is applied. The rectangular computational domain $[-7, 5] \times [-3.015, 3.015]$ was discretized into 400×201 finite elements each having a side length $h = 0.03$. Infinite elements of order 9 were used along the outer boundary. The material interface was set along the line $x = 0$, and the fluid source was set at $x = -1, y = 0$ (see Fig. 20). The initial solution for the horizontal crack of half-length $\gamma_L^1 = \gamma_R^1 = 0.5$ was set according to the viscosity-dominated M-vertex solution [18,19]. The fracture was then propagated for 25 steps assuming a variable time-step. For the case when $E_2/E_1 = 0.5$, an

adaptive time-step was chosen so that the expected crack front advance at the crack tip approaching or crossing the interface is approximately equal to 0.1, that is $\Delta\tau = 0.1/\dot{\gamma}_R$, where $\dot{\gamma}_R$ is the crack front velocity at the previous time-step for the crack wing to the right of the fluid source. To compare the solutions for $E_2/E_1 = 0.5$ and $E_2/E_1 = 0.2$ at the same times, we set the same time-steps for $E_2/E_1 = 0.2$ as those obtained when using the adaptive time-stepping for $E_2/E_1 = 0.5$. The relative tolerance for the locating the fracture front was set to $\delta_\gamma = 10^{-3}$. As before to avoid the instabilities associated with extremely small elements along the crack that can result from an awkward intersection of the crack with the underlying FEM mesh, we ensured that the size of the tip region Σ_t at each crack tip was no smaller than $h/3$; thus one or two tip elements per crack wing were used at each time-step.

Fig. 22 shows snapshots of the computed crack width and the fluid pressure, together with the M-vertex solution [18,19] that is associated with the case when $E_2/E_1 = 1$. The interface is located at $\zeta = 1$ in this figure. For each value of the ratio E_2/E_1 the fracture volume is equal to the dimensionless time τ .

At the first time-step ($\tau = 0.95$), the fracture is within material I and the crack has had very little time to evolve from the initial solution, which is assumed to be symmetric, thus the crack width

is approximately same as in the symmetric initial solution. When the fracture crosses the interface, as expected, the fracture opening is larger in material II because it has a smaller Young's modulus. We note that since each of the cases is sampled at the same time, volume conservation dictates that each of the fractures should include the same volume. The bi-material crack propagates more rapidly into the softer region than in the homogeneous case. In addition, because of the herniation effect in the softer region, the right moving wing of the fracture accepts more fluid than the left moving wing, which is relatively starved of fluid and therefore has a crack front that moves more slowly. We note that as a result of this herniation effect, the progress of the left moving front becomes markedly less as the ratio E_2/E_1 decreases, while this difference between the front positions for the right moving fronts is much less in the softer medium.

Since there is no reference solution for this problem, we performed several tests to check the accuracy of the results. We modeled the same problem with $E_2/E_1 = 0.2, 0.5, 1$ and with a larger mesh-size $h = 0.05$ to identify the level of accuracy with respect to the finite element mesh. The solution with $E_2/E_1 = 1$ was compared with the M-vertex solution. Even for this homogeneous case, for which the solution should be symmetric, it is possible to induce a small asymmetry in the XFEM solution if the crack is initiated too close to the infinite element boundary. This problem can be eliminated if the computational domain is centered on the fluid source and there is a sufficient distance between the source and the finite element-infinite element boundary. For this reason, for the results presented in the plots provided, we used a computational domain that was centered at the fluid source. It is interesting to note that the results for $E_2/E_1 = 0.2, 0.5$ do not change noticeably between an asymmetric location of the source within the computational domain and when the source is centered at the origin $x = y = 0$ of computational domain. This is because the asymmetry in the bi-material solution dominates any minor asymmetry that might be introduced by the crack coming too close to the infinite element boundary.

We then performed simulations with increased and decreased time-steps to test convergence of the results for the time when the crack tip is approaching and crossing the interface. Indeed, the viscous tip asymptote (39) applies when the immediate neighborhood of the crack tip is contained within a homogeneous part of the domain and is not tailored to the case when the crack tip is near a bi-material interface. Naturally, if the time step is so large that the crack front moves over several elements including the interface itself, then one would expect significant errors to result. However, as the crack fronts move away from the interface, these errors attenuate and the solutions move closer to those obtained with smaller time-steps.

5. Conclusions

In this paper we have described two P&W XFEM schemes that use a novel implicit level set algorithm to resolve the singular free boundary problem for HF propagating without a fluid lag. The level set scheme is able to accommodate fracture front advances that can be asymmetric. This algorithm is able to make use of the local asymptotic behavior to locate the unknown free boundary and is particularly useful for singular free boundary problems in which calculating the fluid velocity involves evaluating an indeterminate form. To demonstrate its versatility in this regard, we use the ILSA scheme to capture HF propagation for a wide range of values of the dimensionless toughness \mathcal{K} . These correspond to points along the MK edge of parameter space [2] associated with quite different regimes of propagation and asymptotic solutions close to the fracture tips. To achieve this the algorithm uses the universal asymptote of

Garagash [3] and Garagash and Detournay [4], which is derived by considering a semi-infinite HF propagating with a constant velocity V .

The two P&W XFEM schemes differ in the way in which the tip enrichment and the tip asymptotic behavior is implemented. The tip enriched scheme *XFEM-t*, makes use of sign enrichment to represent the geometry of the crack in the channel region, tip enrichment around the tip regions with a power law that is consistent with the current propagation regime of the HF, and blending at the interface between these two enrichments. The union of these two enrichment regions coincides with the current crack curve. This scheme imposes the asymptotic behavior as a boundary condition in the tip region and uses the pressure field derived from a finite volume solution to the lubrication equation in the channel region. The *XFEM-t* scheme also requires that the computationally intensive singular enrichment integrals be updated at each new trial position for the crack tips. To avoid this costly exercise, we also considered the simpler *XFEM-s* scheme, which does not require specialized tip enrichment and for which the geometry of the crack is defined throughout by sign enrichment. The *XFEM-s* enrichment not only encompasses the crack but may also extend beyond the actual crack tips to the edge of the nearest element in the FE mesh. The asymptotic behavior in the crack tip is only applied in a weak sense by imposing the asymptotic behavior for the intersection of the crack tip region and the last sign enriched elements deemed to be in the tip region. The advantage of this scheme is that it does not require singular tip enrichment and can accommodate a number of front advances in the leading element without updating even the sign enrichment. Naturally, because it incorporates the correct enrichment, the tip enriched scheme is more accurate when required to solve the mixed boundary value problem in which asymptotic tip widths are imposed and pressures are prescribed in the channel. However, this additional precision will not always translate to superior performance of the *XFEM-t* scheme compared to *XFEM-s* scheme, if, for example, the errors due to the infinite elements are not sub-dominant. The convergence rates for the dynamic XFEM schemes are shown to approximately follow those of the static XFEM schemes when solving the corresponding mixed boundary value problem. In particular, the *XFEM-t* scheme achieves an $O(h^2)$ asymptotic convergence rate, while the *XFEM-s* scheme achieves an $O(h)$ asymptotic convergence rate. Given the additional computational burden of the numerical integrations required to implement the *XFEM-t* scheme, the additional accuracy might not be warranted.

XFEM models for fractures in bi-material elastic media were also considered. Comparisons with static reference solutions demonstrated that the XFEM scheme yields extremely accurate results with relatively few resources. The XFEM models of hydraulic fractures propagating in bi-material elastic media demonstrate that the XFEM schemes are able to capture the interesting herniation behavior of the fracture width field in the softer materials and the corresponding effect on the location of the fracture front positions. The proposed ILSA-XFEM schemes demonstrate a robust and flexible framework for discretizing and solving the singular free boundary problems associated with hydraulic fractures propagating without a fluid lag.

Acknowledgments

The MATLAB codes used for numerical simulations in this paper were based on the original MATLAB software package for XFEM implementation in a domain with a crack by Dr.-Ing. T.-P. Fries (RWTH Aachen University), available at www.xfem.rwth-aachen.de/Background/Download/XFEM_Download.php. The authors gratefully acknowledge this resource. The authors also thank Dr. Jose Adachi (Chevron) for sharing the semi-analytic M-vertex and

MK-edge solutions, Professor Dmitry Garagash (Dalhousie University) for sharing the details of the universal crack-tip asymptote, and Professor Emmanuel Detournay (University of Minnesota) for stimulating discussions. This work was partially funded by the NSERC Discovery Grants program, which both authors gratefully acknowledge.

Appendix A. Supplementary data

Supplementary data associated with this article can be found, in the online version, at <http://dx.doi.org/10.1016/j.cma.2013.07.016>.

References

- [1] E. Gordeliy, A. Peirce, Coupling schemes for modeling hydraulic fracture propagation using the XFEM, *Comput. Methods Appl. Mech. Eng.* 253 (2013) 305–322.
- [2] E. Detournay, Propagation regimes of fluid-driven fractures in impermeable rocks, *Int. J. Geomech.* 4 (1) (2004) 1–11.
- [3] D. Garagash, Near-tip processes of fluid-driven fractures, Ph.D. Thesis, University of Minnesota, Minneapolis, 1998.
- [4] D. Garagash, E. Detournay, The tip region of a fluid-driven fracture in an elastic medium, *ASME J. Appl. Mech.* 67 (1) (2000) 183–192.
- [5] A. Rubin, Propagation of magma-filled cracks, *Ann. Rev. Earth Planet. Sci.* 23 (1995) 287–336.
- [6] V.C. Tsai, J.R. Rice, A model for turbulent hydraulic fracture and application to crack propagation at glacier beds, *J. Geophys. Res. Earth Surf.* 115 (2010) F03007, <http://dx.doi.org/10.1029/2009JF001474>.
- [7] R. Jeffrey, K. Mills, Hydraulic fracturing applied to inducing longwall coal mine goaf falls, in: *Pacific Rocks 2000*, Balkema, Rotterdam, 2000, pp. 423–430.
- [8] A. van As, R. Jeffrey, Caving induced by hydraulic fracturing at Northparkes mines, in: *Pacific Rocks 2000*, Balkema, Rotterdam, 2000, pp. 353–360.
- [9] P. Valkó, M. Economides, *Hydraulic Fracture Mechanics*, John Wiley & Sons, Chichester UK, 1995.
- [10] M. Economides, K. Nolte (Eds.), *Reservoir Stimulation*, third ed., John Wiley & Sons, Chichester, UK, 2000.
- [11] U. Frank, N. Barkley, Remediation of low permeability subsurface formations by fracturing enhancements of soil vapor extraction, *J. Hazard. Mater.* 40 (2005) 191–201.
- [12] L. Murdoch, Mechanical analysis of idealized shallow hydraulic fracture, *J. Geotech. Geoenviron.* 128 (6) (2002) 488–495.
- [13] N. Moës, J. Dolbow, T. Belytschko, A finite element method for crack growth without remeshing, *Int. J. Numer. Methods Eng.* 46 (1999) 131–150.
- [14] M. Stolarska, D. Chopp, N. Moës, T. Belytschko, Modeling crack growth by level sets and the extended finite element method, *Int. J. Numer. Methods Eng.* 51 (2001) 943–960.
- [15] N. Sukumar, J.-H. Prevost, Modeling quasi-static crack growth with the extended finite element method. Part I: computer implementation, *Int. J. Solids Struct.* 40 (2003) 7513–7537.
- [16] A.P. Peirce, E. Detournay, An implicit level set method for modeling hydraulically driven fractures, *Comput. Methods Appl. Mech. Eng.* 197 (2008) 2858–2885, <http://dx.doi.org/10.1016/j.cma.2008.01.013>.
- [17] E. Gordeliy, A.P. Peirce, Enrichment and convergence of the XFEM for hydraulic fracture problems, in preparation.
- [18] J.I. Adachi, Fluid-driven fracture in permeable rock, Ph.D. Thesis, University of Minnesota, Minneapolis, 2001.
- [19] J. Adachi, E. Detournay, Self-similar solution of a plane-strain fracture driven by a power-law fluid, *Int. J. Numer. Anal. Methods Geomech.* 26 (2002) 579–604.
- [20] J. Rice, Mathematical analysis in the mechanics of fracture, in: H. Liebowitz (Ed.), *Fracture, an Advanced Treatise*, vol. II, Academic Press, New York, NY, 1968, pp. 191–311 (Chapter 3).
- [21] J. Desroches, E. Detournay, B. Lenoach, P. Papanastasiou, J. Pearson, M. Thiercelin, A.-D. Cheng, The crack tip region in hydraulic fracturing, *Proc. R. Soc. London, Ser. A* 447 (1994) 39–48.
- [22] A. Zilian, T.-P. Fries, A localized mixed-hybrid method for imposing interfacial constraints in the extended finite element method (xfem), *Int. J. Numer. Methods Eng.* 79 (2009) 733–752.
- [23] T.-P. Fries, A corrected XFEM approximation without problems in blending element, *Int. J. Numer. Methods Eng.* 75 (2008) 503–532.
- [24] A.P. Peirce, A Hermite cubic collocation scheme for plane strain hydraulic fractures, *Comput. Methods Appl. Mech. Eng.* 199 (29–32) (2010) 1949–1962, <http://dx.doi.org/10.1016/j.cma.2010.02.009>.
- [25] G. Ventura, R. Gracie, T. Belytschko, Fast integration and weight function blending in the extended finite element method, *Int. J. Numer. Methods Eng.* 77 (2009) 1–29.
- [26] I. Babuska, J.M. Melenk, The partition of unity method, *Int. J. Numer. Methods Eng.* 40 (1997) 727–758.
- [27] P. Laborde, J. Pommier, Y. Renard, M. Salaün, High-order extended finite element method for cracked domains, *Int. J. Numer. Methods Eng.* 64 (2005) 354–381.
- [28] J. Marques, D. Owen, Infinite elements in quasi-static materially nonlinear problems, *Comput. Struct.* 18 (4) (1984) 739–751.
- [29] P. Bettess, *Infinite Elements*, Panshaw Press, 1992.
- [30] R. Carbonell, J. Desroches, E. Detournay, A comparison between a semi-analytical and a numerical solution of a two-dimensional hydraulic fracture, *IJSS* 36 (31–32) (1999) 4869–4888.
- [31] F. Erdogan, V. Biricikoglu, Two bonded half planes with a crack going through the interface, *Int. J. Eng. Sci.* 11 (1973) 745–766.
- [32] A. Peirce, E. Siebrits, Uniform asymptotic approximations for accurate modeling of cracks in layered elastic media, *Int. J. Fract.* 110 (2001) 205–239.